TAMPEREEN TEKNILLINEN YLIOPISTO
TAMPERE UNIVERSITY OF TECHNOLOGY

MARTINA BOZIC

TEXTURE OF ECAP PROCESSED ALUMINUM

Master of Science Thesis

Examiners: Professor Veli-Tapani Kuokkala and Dr. Mikko Hokka
Examiners and topic approved by the Council of the Faculty of Engineering Sciences on 5th November 2014

ABSTRACT

TAMPERE UNIVERSITY OF TECHNOLOGY
Master's Degree Programme in Materials Science
BOZIC, MARTINA: Texture of ECAP processed aluminum.
Master of Science Thesis, 66 pages, 65 Figures
Date: 5th November 2014
Major: Materials Science
Examiners: Professor Veli-Tapani Kuokkala and Dr. Mikko Hokka
Keywords: X-ray diffraction, texture measurement, pole figures, aluminum, ECAP

In this thesis the studied material was pure aluminum that was processed by Equal Channel Angular Pressing (ECAP). The main research objectives were to determine the texture development of aluminum during ECAP processing, and to study the changes in texture after additional high rate axial compression deformation. Since aluminum is used quite extensively in many industrial applications it is important to get a better understanding of its micro-structural changes under different loads; and possibilities that might be gained.

The texture measurements were done using X-ray diffraction (XRD) in parallel beam geometry, and the compression tests were done with Split Hopkinson Pressure Bar device (SHPB) at room temperature. The tested samples were processed by ECAP one, four, and sixteen passes.

The results are presented as pole figures for different lattice planes (111), (200) and (220); and as a 3-dimentional orientation distribution functions (ODF's). Based on the results, the texture changes significantly depend on how many times the sample is pressed through the ECAP die. Furthermore, the axial compression deformation affects the texture quite dramatically and this change is stronger for the samples with higher number of ECAP passes.

During the work, several practical issues had to be solved and are also included in this paper. The issues were related to the effect of sample preparation and adjustments on the XRD device during the measurements (2θ angle and the defocusing error). The effects of experimental variables are explained in details and their significance is presented and elaborated in the results.

Preface

The research work for this thesis paper was carried out at the Department of Materials Science of Tampere University of Technology during 2014. I wish to express my deep gratitude to my supervisors Professor Veli-Tapani Kuokkala for trusting me with this research topic and agreeing to be my supervisor for this thesis work; and Dr. Mikko Hokka for his constant guidance, advices, support, inspiring collaboration and encouragement to go deeper into the research matter.

I would also wish to thank several of my colleagues at the department of Materials Science who helped me with performing the experimental parts of the thesis and with whom I had shorter or longer discussions about different parts of this work. Firstly I wish to mention Ahmad Mardoukhi who was a big help with the Split Hopkinson Pressure Bar testing and result analysis. Then, Tuomo Nyyssönen and Leo Hyvärinen for being a constant support regarding any matter related to the x-ray diffraction device setup.

I am also really thankful to my friends Ezgi, Jatin, Burak and Marlitt for constant support and encouragement during the time this thesis was made.

In the end I wish to thank my family, without their support and interest in my studies this wouldn't be possible. Most of all, I thank Tanja for believing in me and encouraging me to take on this challenge in the first place.

Table of contents

Terms and definitions

Crystal symmetry	The crystal can be rotated in different directions without physically changing its properties.
Fibrous structure	The structure consists of crystals that are greatly elongated and have a small cross section.
Lamellar structure	Structure composed from fine, alternating layers of different types of materials or single material in the form of lamellae.
Monochromatic radiation	Electromagnetic radiation that ideally comprise of one single wavelength.
Peak broadening	Peak broadening plays a critical role in the separation of the composition components in a sample and generally peak broadening lowers the resolution.
Reflection geometry	The resulting image is obtained by a reflection and it shows a mirror image of the original object.
Superplasticity of metals	State in which a solid crystalline material is deformed beyond its usual breaking point. During tensile deformation it can elongate over 200%. This is especially the case in fine-grained structures deformed under low strain rates and elevated temperatures.
Sample symmetry	Statistical symmetry and directly related to the deformation that was introduced to the sample.
Stereographic projections	Mapping tool for projecting the upper part of the sphere on to a plane. The reason for this was to enable writing down 3D systems as 2D so that they can be marked on paper.
Texture	Distribution of the grains in preferred orientation in a polycrystalline material.

ABBREVIATIONS

ARB.....Accumulative Roll Bounding
CCDF.....Cyclic Close Die Forging
ECAP.....Equal Channel Angular Pressing
ED.....Extrusion Direction
HPT.....High Pressure Torsion
ND.....Vertical Direction
NSM.....Nano Structured Material
OD.....Orientation Distribution
ODF.....Orientation Distribution Factor
SD.....Shear Direction
RCS.....Repetitive Corrugation and Straightening
REC.....Reciprocating Extrusion-Compression
SHPB.....Split Hopkinson Pressure Bar
SP.....Shear Plane
SPD.....Severe Plastic Deformation
TD.....Transverse Direction
UFG.....Ultra Fine Grain
WIMV.....Williams-Imhoff-Matthies-Vinel
XRD.....X-Ray Diffraction
d.....Diameter
d.....Interplanar spacing of the crystal planes
D.....Detector
l.....Length
n.....Order of the reflection
N.....number of pressing passes
r.....Adjustable radius
R.....Fixed radius
λ.....Wavelength of the incident X-rays
γ.....Shear Strain
ε.....Von Mises Equivalent Plastic Strain
θ.....Scattering angle
ψ.....Axis in the direction of Psi
ϕ.....Axis in the direction of Phi
2θ.....Bragg angle
ψ and ϕ.....Angles of the ECAP die

1. Introduction

1.1 Research Aims

The focus of this study was the development of the deformation texture as a result of severe plastic deformation (SPD). The studied material was pure aluminum that was processed by Equal Channel Angular Pressing (ECAP). This method reduces the material's grain size to submicrometer level by repetitive pressing of the sample through two channels intersecting each other at an angle of 90° to 120°. As a result, large plastic strains are introduced into the material. In this way, because of the reduction of the grain size and increased dislocation density, the material gains very high strength. Since aluminum is one of the basic materials used in many industrial applications there has been an increased interest for better understanding of the possibilities that can be gained through materials processed by SPD methods.

ECAP has a large variety of parameters that will affect and enable control over the texture development. The determination of crystallographic texture is quite complex because of the all possible strain paths that can be performed with this method. Thus the main aims of this research were the determination of the initial texture of the ECAP´ed samples and the comparison of the initial texture with the texture after introducing additional axial compression deformation.

The texture of the ECAP'ed aluminium was first measured using X-ray diffraction (XRD). After that the samples were subjected to additional axial compression deformation using Split-Hopkinson Bar device, and the resulting crystallographic textures were measured again with XRD.

1.2 Thesis Outline

Chapter 2 gives an extensive theoretical background for better understanding of severe plastic deformation (SPD) and its effects on metals. The Chapter also describes the Equal Channel Angular Pressing (ECAP) method and the X-ray Diffraction (XRD) techniques for crystallographic texture determination. First, a general definition of SPD and different SPD methods available for developing of bulk nanomaterials are given in Chapter 2.1. Then Chapter 2.2 introduces the ECAP method with a short discussion about the effects of different parameters related to the method (geometry of the dies, processing routes, pressing speed and corresponding strain). This will be followed by a more detailed introduction to the texture development in pure aluminum during ECAP in Chapter 2.3. This Chapter discusses issues such as what kind of deformation happens, how does the texture develop, and how does the material behave depending on the number of passes through the dies. The Chapter focuses only on the texture development of FCC metals. Chapter 2.4 gives a brief introduction to the main terminology

used in the XRD texture measurements, the main laws and principles, and explanations of the variables that need to be kept in mind when doing this type of measurements. Furthermore, this Chapter covers some specific issues related to XRD texture measurements that should be discussed before the experimental Chapter.

The experimental part provides a short introduction regarding the samples and the used methods. Chapter 4 presents the effect of three different variables (2θ angle, defocusing error, and the sample preparation) on the measurement results, the results and a short analysis. Also the compression tests are described and analyzed in Chapter 5. This is followed by a detailed discussion of the texture measurements results. The thesis finishes with a summary of all relevant conclusions that can be drawn from the presented results and the discussion. Appendices 1, 2 and 3 contain the original texture measurement results before and after the compression testing.

2. THEORETICAL BACKGROUND

2.1 Severe plastic deformation (SPD)

Severe plastic deformation (SPD) is one of the methods used to make ultra-fine grained (UFG) bulk metals and alloys. This is done by introducing very high plastic strains to the metal material, resulting in improved mechanical properties that enable the development of light weight components with high strength (1). Developing a finer grain size, with the increase in strength, also provides higher fracture toughness and the potential for superplasticity. There are other methods beside the SPD that can produce UFG materials (fast solidification, vapor deposition, and high energy ball milling) (1). However, SPD has an advantage over the mentioned methods because it enables over-coming of certain problems that occur in other nano-structured material (NSM) tech-niques, e.g. residual porosity problems that occur in compacted samples or impurities from processes such as ball milling (2). Furthermore, according to Valiev (2) there are three main requirements that have to be fulfilled when dealing with nanostructured ma-terials. Firstly, there should be high angle boundaries because otherwise there will be no qualitative changes in the material's properties. Secondly, the structure must be uniform through the whole sample so that the material has stable properties. Thirdly, the large plastic strains must not initiate internal damage or cracks. Classic methods such as drawing, extrusion or cold rolling cannot meet these requirements. However, through classic methods large plastic deformations can be gained. Large plastic deformations that are gained through classic techniques result in cellular or fibrous structures and they contain mostly low angle boundaries. This is because there are no changes in the strain path during the deformation, i.e. the deformation always accumulates in one direction only. The fibrous structure contains elongated grains with a very small cross section and the cellular structure is made of small crystals. However, during SPD there are possible changes in the strain paths and the structures that are produced are granular (misoriented fine grain) with high angle boundaries (2). Granular structure is developed in the way that the grains first become elongated due to the plastic deformation. After that there is an increase of high angle boundary area as a result of a mechanism called subdivision of grains. In that mechanism the grains will start to break into cells and the structure will develop towards lamellar. Lamellar structure is characterized as containing extremely small grains. In the end the elongated grains will split up as a result of changing of the strain path (3). Granular structure can also be gained from fibrous structure as long as there is a regular change in the strain path. The strain path changes are explained in more details in Chapter 2.2.3.

2.1.1 Severe Plastic Deformation Techniques

Experimental techniques that are typically used for SPD include high pressure torsion (HPT), equal channel angular pressing (ECAP), accumulative roll bonding (ARB), reciprocating extrusion-compression (REC), cyclic closed die forging (CCDF), and repetitive corrugation and straightening (RCS) (4). Figure 1 shows a schematic representation of these methods.

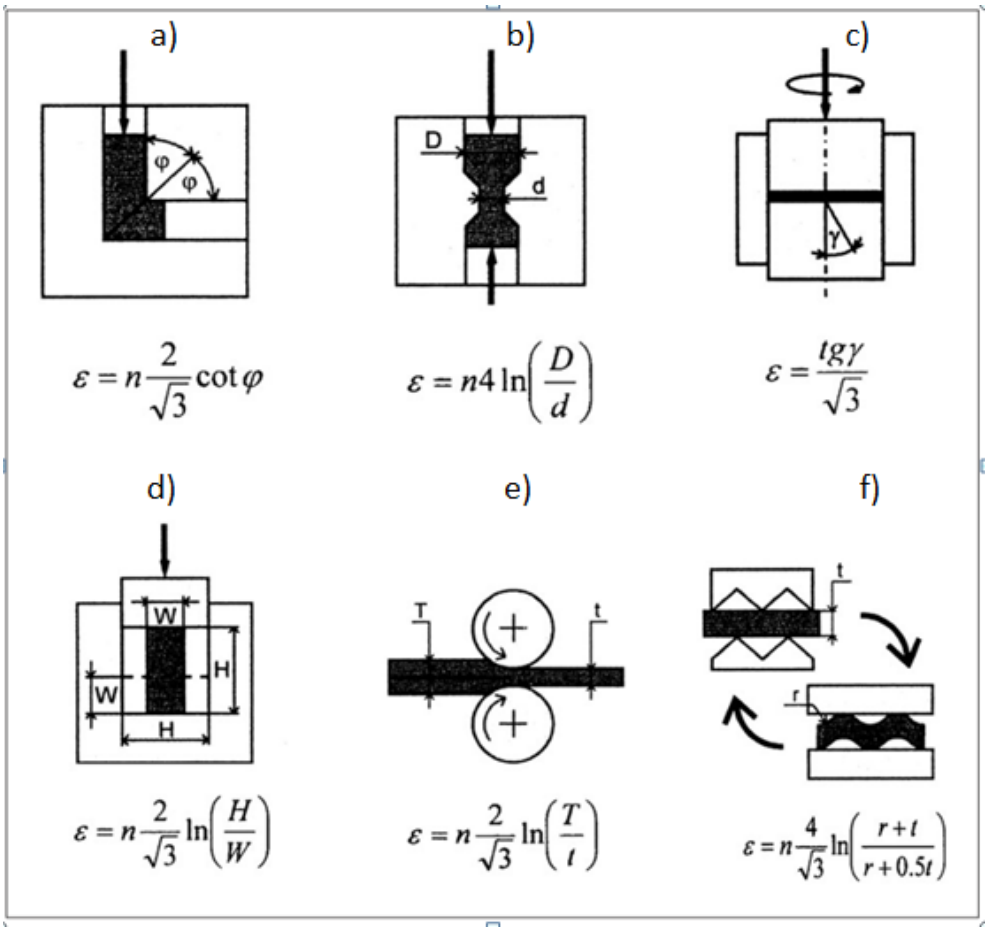

Figure 1: Severe plastic deformation (SPD) methods: a) ECAP, b) REC, c) HPT, d) CCDF, e) ARB and f) RCS (4)

These SPD methods are able to provide large plastic deformation with significantly less material or tool failure limitations than the classic techniques. Furthermore, with some SPD methods, such as equal channel angular pressing (ECAP) it is possible to deform the material without major changes in the size or shape of the billet. This is the main reason why the sample can be re-inserted into the die and pressed multiple times. This is not possible with methods, such as accumulative rolling or drawing (multi-pass) where large plastic deformations can be achieved but as a result the billets are not necessarily in the required forms (4).

2.1.2 Fabrication of bulk nanostructured materials

Nanostructured materials can be obtained from different metals and alloys with the SPD methods. The characteristics of the fabrication of the nanostructured material (NSM) depend on the SPD method, the initial grain size and microstructure, and on the phase composition of the sample (2). The biggest advantage in producing NSM with SPD is the large strains that, with all the previously mentioned facts, contribute to the refining of the microstructure without changing the shape of the billet. However, when it comes to texture development there are some small drawbacks that are still under research. Unlike with conventional material processing, such as cold rolling, where it is possible to control the texture of the finished material, with SPD methods there are still many unknown factors in how to control it (5). Texture patterns can be quite complex even in simple cases. The following Chapter will describe the ECAP method in details and the texture development of face-centered cubic (FCC) metals.

2.2 Equal Channel Angular Pressing (ECAP)

The basic idea behind this method is deformation of the material by simple shear. This method is much more advanced compared to other SPD methods. The reason for that is because it is simple, applicable to a wide selection of metals and alloys with different crystal structures, and to many other materials starting from precipitation hardened alloys to metal-matrix composites. As a result of ECAP the billets preserve quite good homogeneity despite the high strains involved, and relatively large billets can be produced. Therefore, there is a good potential for production of ECAP processed materials that can be used in structural applications (6). There is huge potential for the development of ECAP usage in commercial procedures of metal processing if the process can be scaled-up for pressing of large samples (7). Furthermore, since very large plastic strains are introduced into the material billets, as a result changes on the sub-micrometer lever will occur (grain size refinement of the polycrystalline material to a submicron or nano size scale) and the material will obtain quite unique properties (8).

The device is made of two main components: the plunger and the die. The plunger pushes the sample through the die at controlled pressing speed (9). The schematic presentation of the ECAP device can be seen in Figure 2.

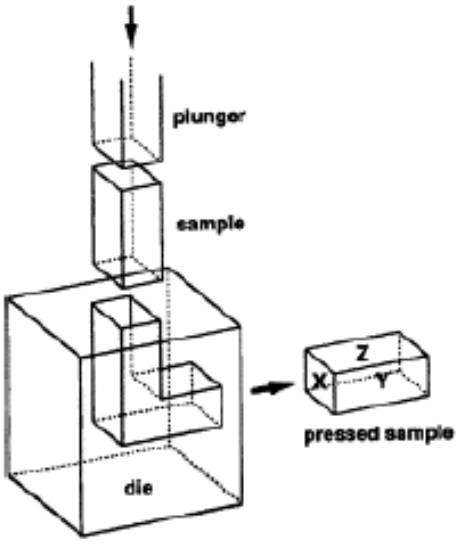

Figure 2: Schematic picture of an ECAP device (9)

This is a discontinuous process that requires inserting and re-inserting the sample into the die. The die is constructed from two channels that have the same cross section (which can be square or circular) and are intersecting at an angle ϕ that can be within the range of 60̊ to 150̊, most often it is 90̊ or 120̊ (Figure 3). Since the sample's cross section does not change it can be re-inserted into the die and more plastic strain can be applied.

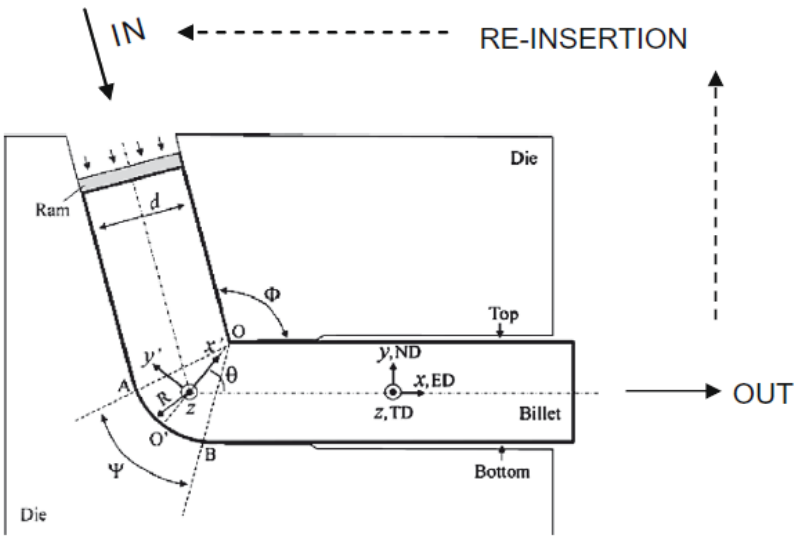

Figure 3: ECAP die geometry (10)

When the sample is re-inserted it should be rotated in order to align it again with the entry channel, and this will result in strain path change on the sample with each pass (11). When the sample passes the intersection point of the two channels the material deforms by simple shear before exiting the die. Each part of the pressed sample has a name to avoid confusion as can be seen in Figure 2. The extrusion direction is ED, the

transverse direction is TD, and the vertical direction relative to the axis of the billet is ND (12).

2.2.1 Geometry of the dies and process parameters

The geometry of the ECAP equipment refers to the intersection angle of the two channels (angle ϕ) and the position where the arc of the curvature is positioned (angle ψ) (Figure 4). The values for the intersection angle ϕ were already mentioned, and for the arc of the curvature, ψ, it must be within the range $0^\circ \leq \psi \leq (180^\circ - \phi)^\circ$.

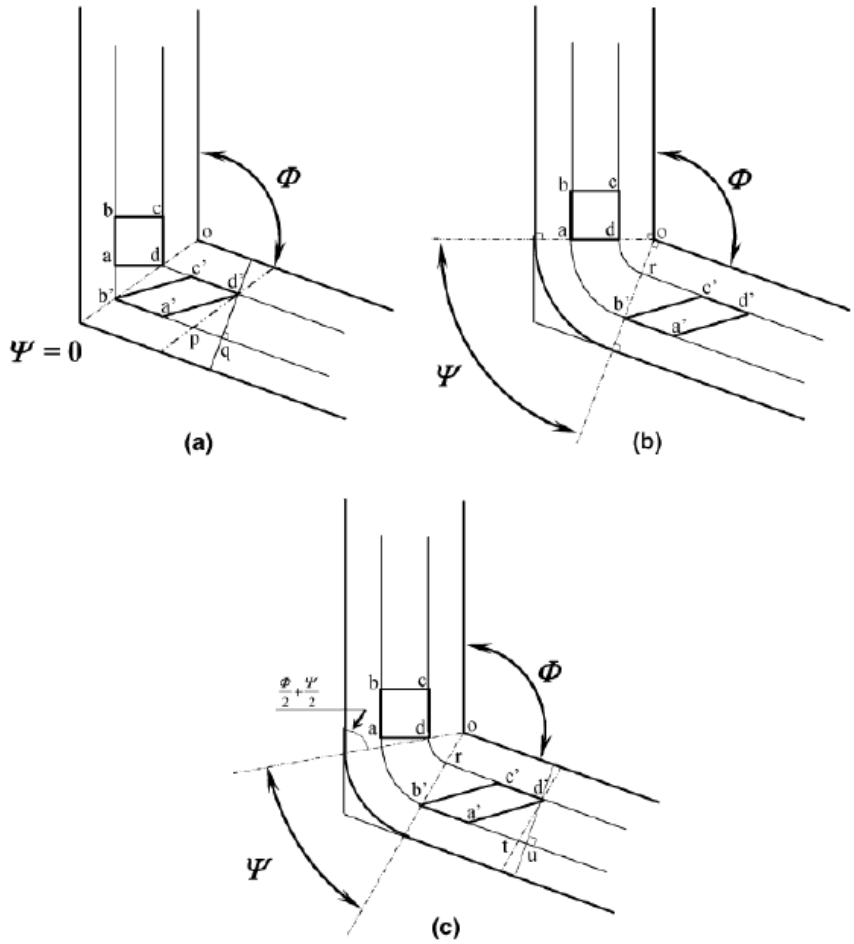

Figure 4: Schematic picture of different ECAP die geometries depending on the values of the inner and outer angles (13)

Under ideal conditions (when the sample in the die is lubricated and there is no friction) the simple shear strain, which is introduced to the billets, is a function of the two mentioned angles. This can be described by Equation (1). However, the Von Mises strains are a bit different because the number of the pressing passes, N, is taken into account and the shear strain is divided by $\sqrt{3}$ to obtain the equivalent strain in Equation (2) (13). It is understandable that with smaller angles of the channels there will be larger imposed strain on the sample. In the following Equations, γ is the shear strain, ε is Von

Mises equivalent plastic strain, ψ and ϕ are the angles of the die, and N is the number of the pressing passes.

$$\gamma = 2\cot\left(\frac{\phi}{2}+\frac{\psi}{2}\right)+\psi\mathrm{cosec}\left(\frac{\phi}{2}+\frac{\psi}{2}\right) \quad (1)$$

$$\varepsilon = \left(\frac{N}{3^{1}/_{2}}\right)\left[2\cot\left(\frac{\phi}{2}+\frac{\psi}{2}\right)+\psi\mathrm{cosec}\left(\frac{\phi}{2}+\frac{\psi}{2}\right)\right] \quad (2)$$

Besides the angles, the pressing speed and the back pressure should also be considered. If the pressing speed is kept low, the microstructure will be more balanced because there will be less recovery. If high speed is used and the sample material is pure aluminum, the temperature will rise because of the adiabatic heating. Higher temperatures during pressing will lead to increased grain size and higher amount of low angle grain boundaries. This is a result of faster recovery that leads to a higher probability of dislocation annihilation (14).

Back pressure is developed by increasing the friction in the exit channel or by adding another plunger, which is positioned in front of the exiting sample. With back pressure it is possible to control the uniformity of the metal flow (more uniform distribution of strain) and the so called *"dead zone"* is avoided (15). The dead zone is formed in the corner area of the dies as can be noticed in Figure 4(c). As the sample passes through the die, larger strains will develop in the inner angle than in the outer one. This will result in an inhomogeneous strain distribution across the sample cross section (16). In conclusion, to achieve optimum UFG material, ECAP method should be done at the lowest possible temperature, low plunger speed and with back pressure.

2.2.2 Processing routes and the shear plane

Between the passes, the samples are usually rotated by 0˚, 90˚or 180˚ around the longitudinal axis. However, the ECAP routes have a specific pattern of rotation that they follow during the process. There are four different types of routes, as shown in Figure 5: route A where the sample is pressed without any rotation; route B_A where the sample is first rotated clockwise by 90˚ and then anti-clockwise by 90˚; route B_C has no changes in the rotation direction, the sample is always rotated in the same direction by 90˚, and route C where the sample is always rotated in the same sense by 180˚ (17). However, one should keep in mind that the routes are not limited only to the mentioned four if the samples in question are circular cross-section billets. However, the same routes are generally applied in cases of circular cross-section samples, too (7).

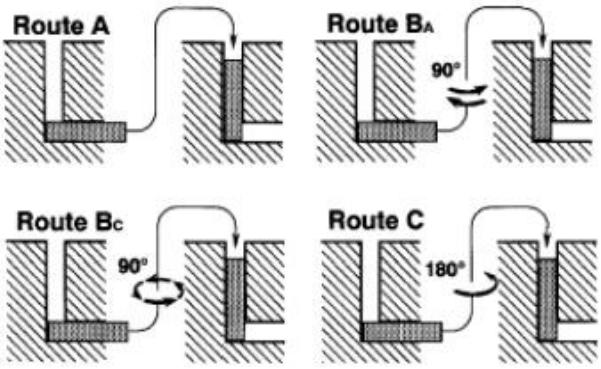

Figure 5: Different types of processing routes for ECAP (17)

The importance of different routes is that they all lead to different shear directions during the deformation. In Figure 6 the shear directions/planes are presented for all four ECAP routes (18).

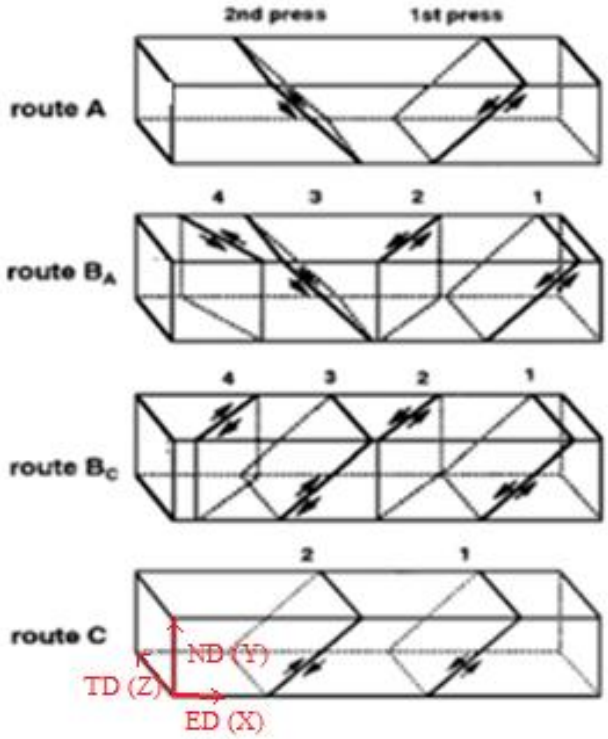

Figure 6: Shear planes indifferent ECAP routes (18)

In order to make Figure 6 more understandable, a so called *"virtual continuous ECAP process"* was developed. In this virtual concept (Figure 7), the ECAP process is observed as a continuous process. It can be estimated only virtually since the friction forces would be too high for a plunger to push a sample through this kind of die construction. As the sample is being rotated after every pass in the conventional ECAP process, for this model the ECAP die is simply reverse-rotated and the dies are connected (19).

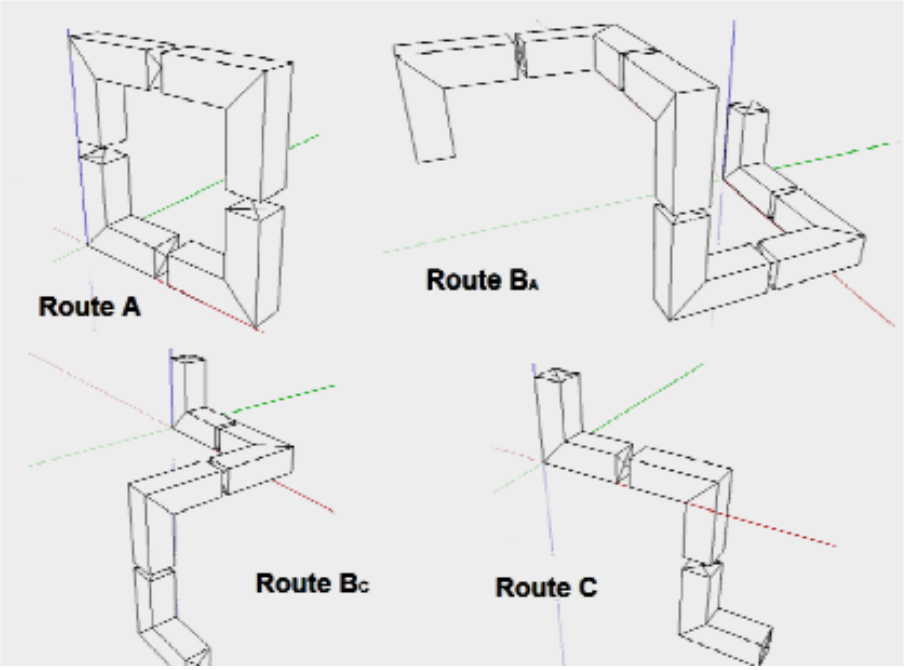

Figure 7: Virtual continuous ECAP process in 3Dand the corresponding shear planes (19)

Using Figure 7 and comparing it with Figure 6 it makes much more sense how the shear planes are changing directions depending on the rotation of the sample. In route A, the intersection of the two neighboring planes is less than 90˚; in routes B_A and B_C the angle between the shear planes is 60˚; and in route C the angle of intersecting the shear planes is 180˚. In the routes B_C and C the shear is reversed since the shear strain will be more or less fully recovered. For that reason these routes are referred to as redundant strain processes. Routes A and B_A will have quite an opposite effect, where the strain will cumulatively build up with each turn (19).

2.3 Texture evolution in FCC metals during ECAP

Before discussing the texture evolution deeper, the basic terminology should first be explained. Texture, in general, is the preferred distribution of crystal orientations (grains) in a crystalline material (20). One of the ways to describe texture in FCC materials as a result of ECAP is through texture fibers. For FCC crystal structures the most important ones are α and β fibers, as shown in Figure 8 (21). They present the texture as a line within the Euler orientation space in a way that the fiber connects different deformation texture components. As presented in Figure 8, Euler space represents a three-dimensional space of a rigid body with unique Euler angles (φ_1, ϕ and φ_2) for every component within the space. An example of these texture components can be observed in Figure 8 and Table 1.

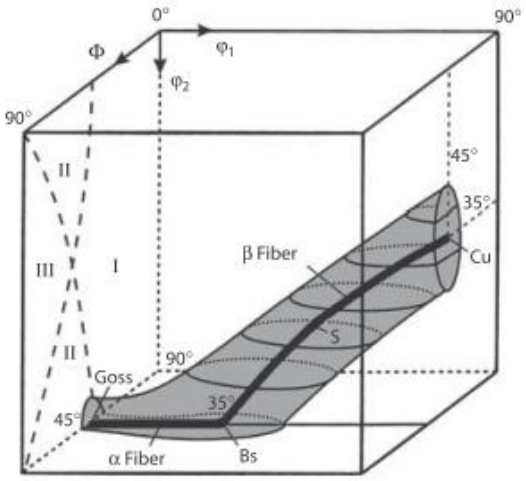

Figure 8: Position of the α and β fibers in Euler space of rolled FCC metal (21)

Table1: Ideal texture components of rolled FCC metal (22).

		Euler angles					
		Roe ψ, θ, ϕ					
Component	$\{hkl\}\langle uvw\rangle$	Matthies α, β, γ			Bunge[a], $\varphi_1, \Phi, \varphi_2$		
Cube, □	$\{001\}\langle 100\rangle$	0	0	0	0	0	0
Copper, ○	$\{112\}\langle 11\bar{1}\rangle$	180	35	135	90	35	45
S, ×	$\{123\}\langle 63\bar{4}\rangle$	211	37	117	59	37	63
Brass, ●	$\{110\}\langle \bar{1}12\rangle$	35	90	135	35	45	90
Goss, ◊	$\{110\}\langle 001\rangle$	0	90	135	0	45	90

As can be noted from Table 1, the texture components have names that are given according to the person who found them or the alloy where they are mostly found. They are defined with Miller indexing notations and they have corresponding points in Euler space, fixed values of the three angles. Furthermore, each component can occur in more than just one location because of the sample symmetry (23). It should be noted here that sample symmetry is not the same as crystal symmetry.

The behavior of the crystal structure of FCC metals under ECAP is compared to the one of simple shear deformation. The ideal behavior when dealing with simple shear is usually described with two partial fibers defined as (1 1 1)||SP (fiber α) and (⟨1 1 0⟩)||SD (fiber β). The SP is the shear plane and SD the shear direction (24). Figure 9 shows the ideal FCC fibers in a (1 1 1) pole figure. Pole figures are usually used in texture or crystallography analysis in materials science. They are stereographic projections and they represent the graphical orientation distribution of the crystal lattice planes.

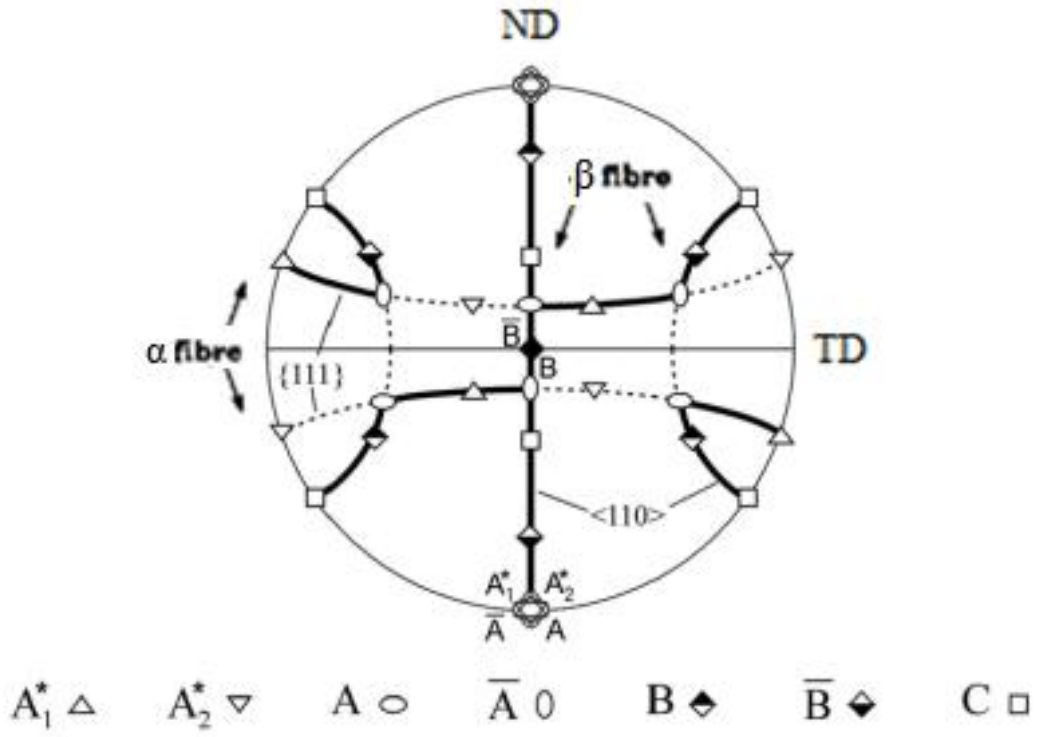

Figure 9: Ideal α and β fibers in simple shear in a FCC {1 1 1} pole figure (10)

As can be observed from Figure 9, along the α fiber the most intense texture components are $A, \overline{A}, A_1^*, A_2^*$, while along the β fiber there are components $A, \overline{A}, B, \overline{B}$ and C. Furthermore, the two fibers are connected in points A and $\overline{A}$ (24). These components will be in the same location for both positive and negative shear. However, negative simple shear will result in partial texture fibers, as can be noticed in Figure 9 marked with thick, solid lines. In simple shear there is a two-fold symmetry that goes around the axis perpendicular (TD axis) to both the shear plane (SP) and shear direction (SD) vectors. In this symmetry, when referring to the intensities of the components, A has about the same intensity as $\overline{A}$, and B has the same as $\overline{B}$. However, the components that are not a part of the 2-fold symmetry (A_1^*, A_2^*) can develop different intensities. Component C is also not compatible with the 2-fold symmetry and exists as a single orientation. These types of orientations are called self-symmetric and can evolve independently from each other (24). In ECAP processed FCC metals the simple shear occurs in the negative sense where component A_2^* is much weaker that component A_1^*.

This simple shear texture is compared with the texture that develops after a single ECAP pass. In the case of a typical ϕ=90° angle of the ECAP process dies, the ideal fiber texture will develop in such a way that the pole figures rotate around the center (around ED axis) by 45° (10). An example is shown in Figure 10, where the ED axis is marked with the red dot.

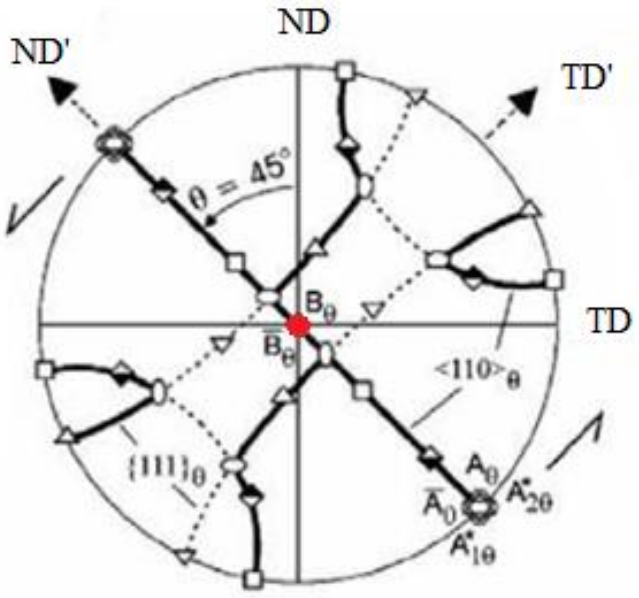

Figure 10: Pole figure {1 1 1} after a single ECAP pass (24)

This relationship between the ideal simple shear and ECAP texture after one pass is even clearer in the Euler space representation, as shown in Figure 11. It is easy to see how all the components are shifted by 45° along φ_1, around the ED axis.

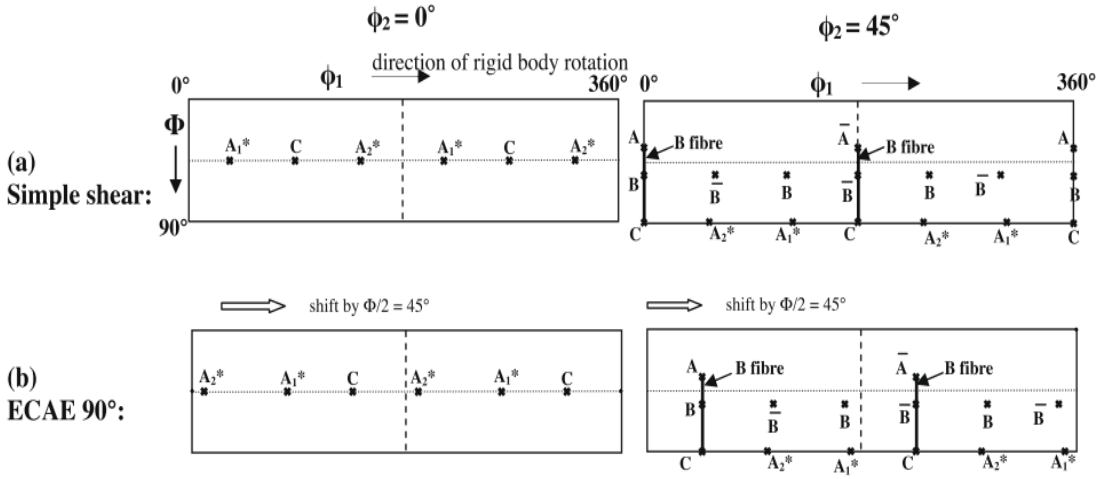

Figure 11: Orientation distribution functions for: a) sample deformed by simple shear; and b) an FCC metal ECAP sample after one pass (24)

In this example, the Euler space is observed as a 2-D system with a fixed angle $\varphi_2 = 0$ and $\varphi_2 = 45°$. The other two angels vary, φ_1 ranging from 0° to 360° and φ ranging from 0° to 90°. This way of using the Euler space is usually used for observing orientation distribution (OD) and is known as OD sections. The reason for that is because it is presented as a series of sections (one box is a section). Each section presents the intensities of the OD for a certain fixed value of φ_2 angle (23).

2.3.1 Texture of aluminum after one and several ECAP passes

After a single ECAP pass, both the microstructure and the texture become very inhomogeneous. This can be observed from Figures 12 and 13, representing the texture development through several pole figures (25). Figure 12(a) shows three pole figures obtained from a 20x20 µm area, which all show prominent texture components (for example: in the case of pure aluminum there are three intensity clusters in the 200 pole figure making one texture component). The other Figures 12(b) and 13 are from a larger area (100x100 µm), and therefore contain more than only three clusters as in the earlier example (25). According to Zhilyaev et al**.** (26), pole figures obtained from the large scan area contain the earlier mentioned α fiber. Furthermore, the pole figure appears a bit different in each region. Figure 13 shows how in some cases (110) is aligned with the shear direction (Figure 13 (b)); while in other (111) will be aligned with the shear direction (Figure 13(a)) (25). The dashed lines in the images represent the shear direction for these examples.

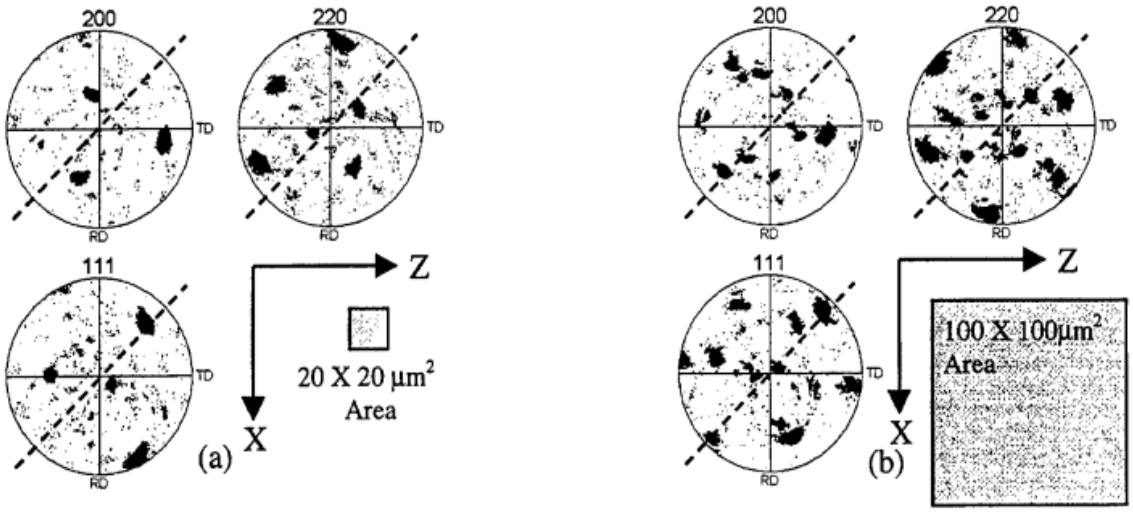

Figure 12: Pole figures after one ECAP pass for pure aluminum obtained from a) a small area and b) a larger area (25).

Additionally it should be noted (Figure 12) that there is a requirement for large and small area measurements in order to obtain accurate representations of the inhomogeneity within the sample (25).

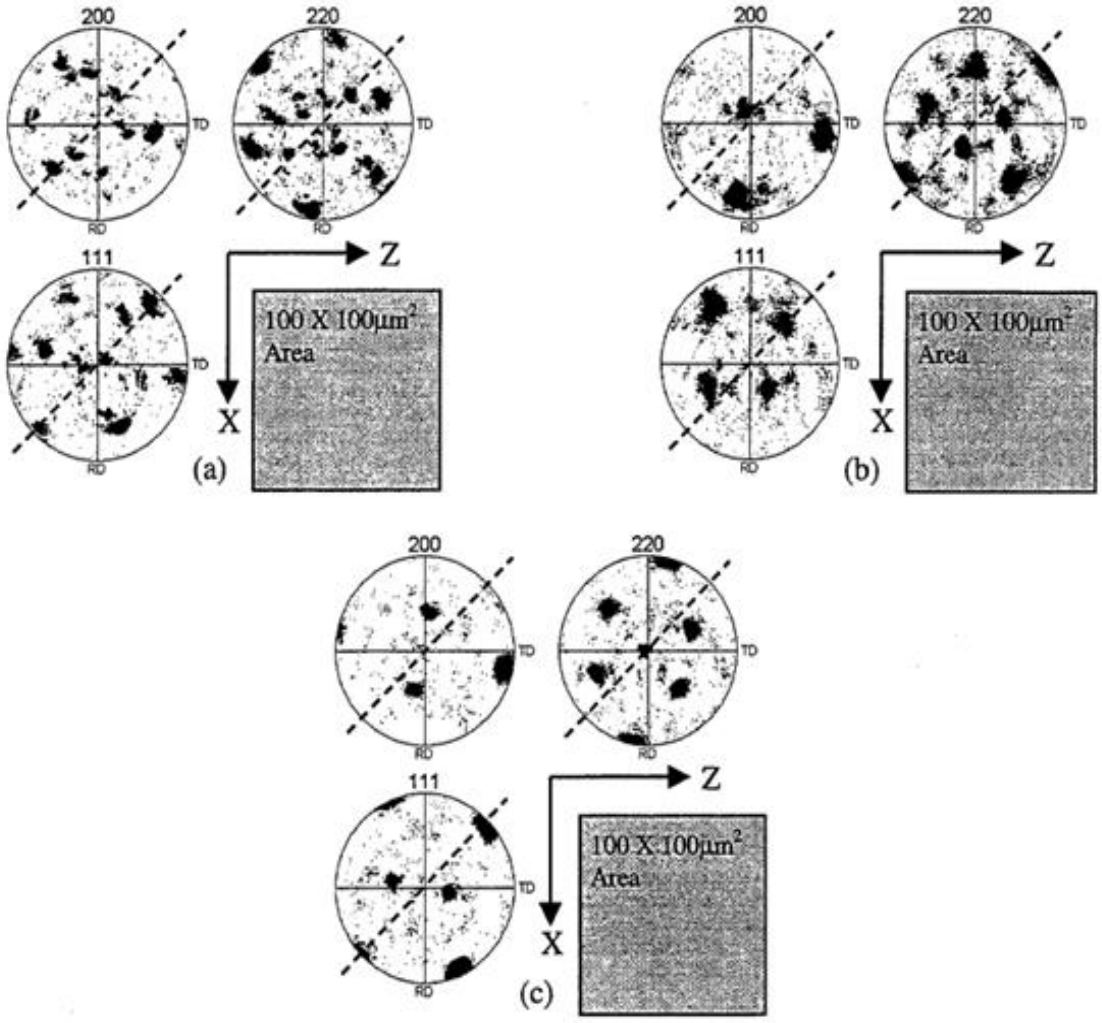

Figure 13: Pole figures for pure aluminum after one ECAP pass showing (a) several intensity clusters; (b) and (c) less clusters (25).

After four ECAP passes the pole figures look more blurry and spread out than after just one pass. Figure 14 shows the data collected from a small (20x20 μm) as well as from a large scanned area processed with different routes: (a), (b) route A; (c) and (d) route B_C, and (e) and (f) route C. In the results obtained from large measured areas (100x100 μm) processed by route A and B_C, it is easy to see a clear, strong tendency for <1 1 1> to align with the shear direction of the last pressing pass (25). At the same time there is a rotational symmetry (Figure 14(f)) around <1 1 1> which is positioned in the shear plane (Y direction in this example).

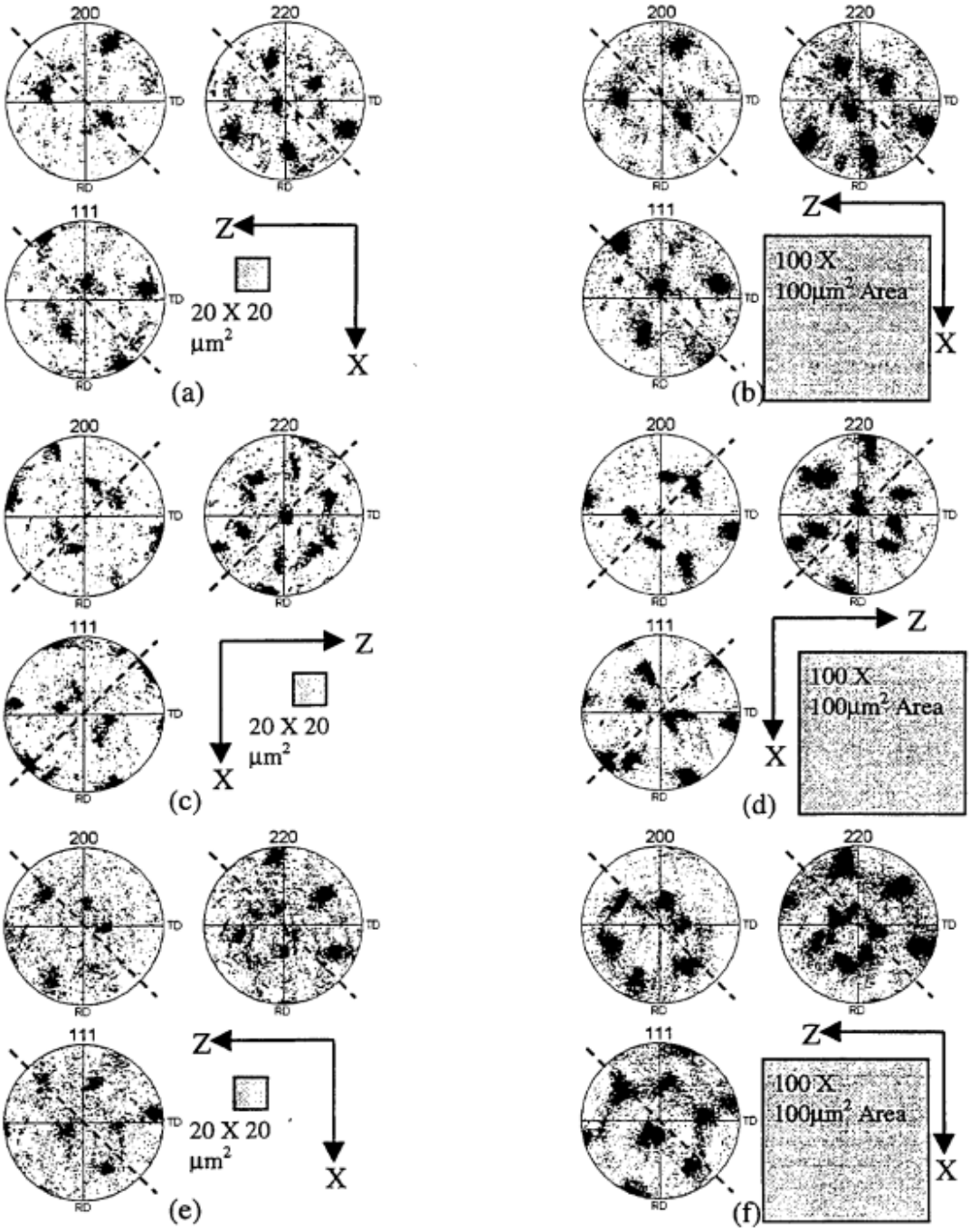

Figure 14: Pole figures after four ECAP passes of pure aluminum: (a), (b) route A; (c), (d) route B_C and (e), (f) route C (25).

Scans from even larger areas than 100x100 μm show multiple texture components, and the relative intensities that are associated with the orientations, are similar to the ones in Figures 14(d) and (f). Figures 14 (d) and (f) show the samples that were processed by routes B_C and C (25). Furthermore, the presence of both α and β fibers can be noticed in Figure 14(b) (25). The scans from the smaller 20x20 μm area show a less spread out texture (in comparison to the larger area from the four ECAP pass) and contain only one dominant orientation (25). Basically the result is as the one obtained after only one

ECAP pass and suggests that there are some features in the microstructure (and also in the meso-scale) that require further measurements on a smaller scale (25).

After 12 ECAP passes (Figure 15), the texture will look even more spread out and it is quite difficult to interpret. In the small scan area the texture components are a bit clearer and easier to notice and analyze (25), unlike in the pole figures obtained from larges area where there are many intensity clusters overlapping each other. The intensity clusters are located at the intersections of α and β fibers (26).

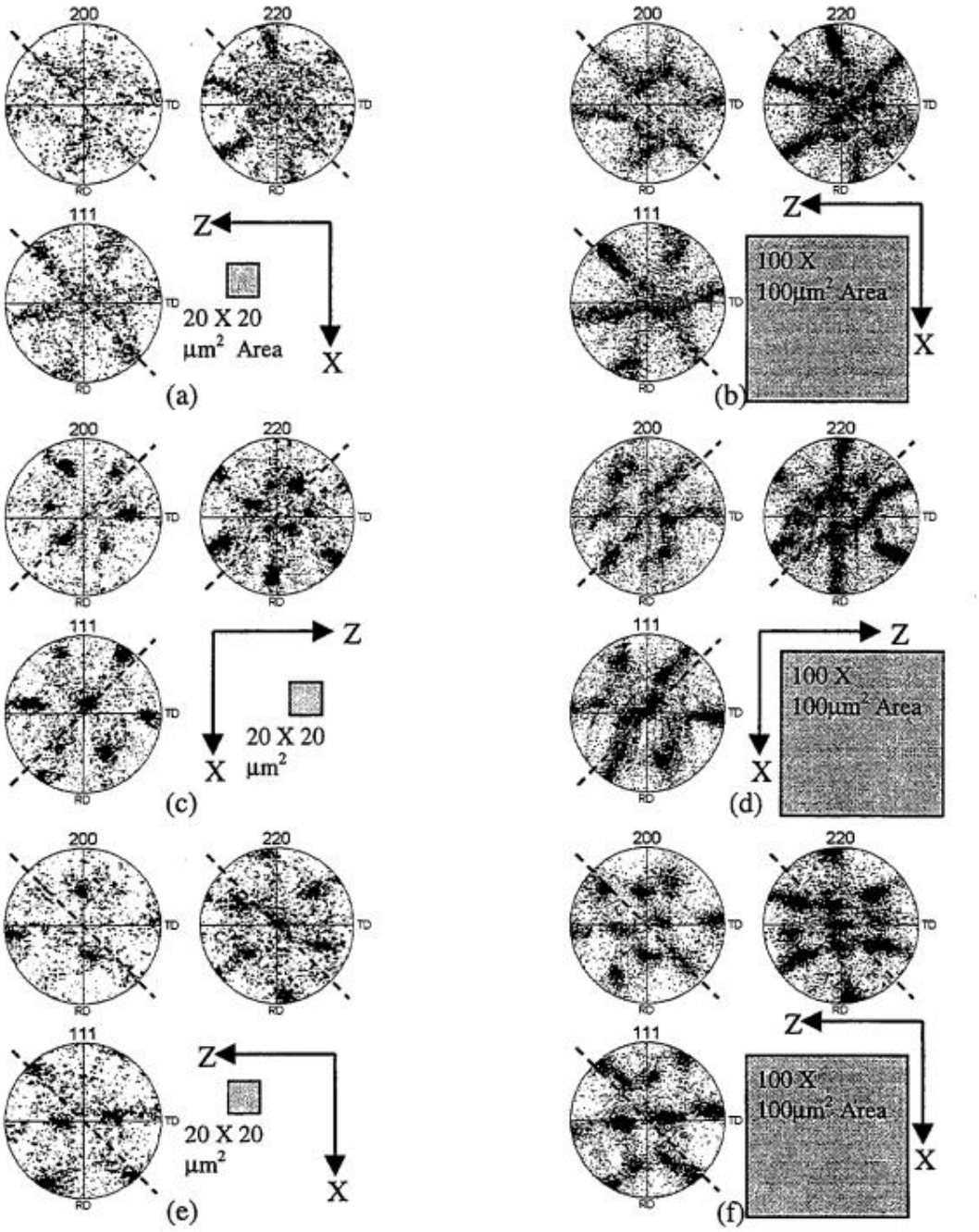

Figure 15: Pole figures for pure aluminum after 12ECAP passes: (a) and (b) route A; (c) and (d) route B_C, and (e) and (f) route C (25).

The larger scans area shows that there is a rotational symmetry around the shear plane normal for all processing routes. This can be best noticed in Figure 15(b) for the pole figure (220), where the sample was processed by route A. In Figure 15(b) there are also overlapping intensity clusters that are perpendicular to the shear plane, and in the case of (111) poles there are intensity clusters parallel to the shear plane. In the example of route B_C (Figure 15(d)), the rotational symmetry can be noticed around the axis normal to the shear plane. However, since <110> is aligned with this axis it results in an increased concentration of components around the normal of the shear plane in the (220) pole figure. Also the (220) pole figure shows a 45˚ rotation to the shear plane (towards TD or Z direction in this example). In the case of <110> rotational symmetry, after route C there is some symmetry but the axis is almost fully aligned with the axis of the pressed billed (ED or X in this example). This will result in an incomplete fiber texture and doesn´t have a continuous distribution when it comes to orientation (25). In all pressing examples it should be noted that (111) has a strong tendency to align with the shear direction (25).

2.4 X-ray Diffraction Texture Measurements

Texture measurements are used to determine the orientation distribution of the crystal grains in a polycrystalline material. One of the most common ways to measure the texture is by X-ray diffraction (XRD), which is an analytical technique where the X-rays scattering from the crystalline object/material are studied. The x-rays diffracting from the sample produce a unique “fingerprint” that is specific to the crystalline structure. The observed information is the X-ray intensity versus the scattering angle (Figure 16) (27). With these kinds of results it is possible to identify and characterize an unknown material (qualitative analysis) by comparing the X-ray pattern of the unknown sample with known diffraction patterns from the library.

Texture analysis is done by measuring the intensities of Bragg’s diffractions as the sample is rotated (phi) and tilted (psi), while keeping the Bragg angle constant. The psi (ψ) and phi (ϕ) angles are shown in Figure 16. The rotation and the tilting movements are achieved with the XRD sample holder. This is done to obtain the intensity at different sample orientations. The results from the measurements, gained by X-ray diffraction method, are plotted as a pole figure (27).

2.4.1 Bragg´s Law and Diffraction

Bragg's law gives the values of the diffracting angles from a crystal lattice (28). It combines the wavelengths of the incident X-rays, the diffraction angle, and the spacing between the crystal lattice planes (29). Bragg´s law is expressed with a simple Equation (3):

$$n\,\lambda = 2\,d\,\sin\theta \qquad (3)$$

where *n* is the order of the reflection, λ is the wavelength of the incident X-rays, d is the interplanar spacing of the crystal planes, and θ is the scattering angle (29). These parameters can also be observed in Figure 17.

When a beam of X-rays hits the atoms of the sample, they will reflect either from the surface or from a plane of atoms inside the crystal. Logically the X-ray that reflects from the atoms inside the crystal will travel longer distance than the one that reflected from the surface. The penetrating X-ray will reflect from one of the internal layers (shown as the crystal lattice planes in Figure 16) and travel the same distance back to reach the surface. That distance will depend on the materials, the angle under which the X-ray entered the material and the interplanar spacing of the atomic planes. Diffraction requires that both the penetrating and the surface reflected waves must are in phase. To make that possible the penetrating wave must travel a certain amount (a whole number) of wavelengths (marked as *n* in Equation c) inside the material. If we observe Equation c), the path difference between the penetrating and the reflected wave is given by $2dsin\theta$, and they will remain in phase because the path length of each wave is an integer multiple of the wavelength. As a result, there will be a bright point on the detector instead of a blurry one (30). Furthermore, the resulting wave will produce a specific diffraction pattern on the detector and each peak on the pattern is known as a Bragg's diffraction (28).

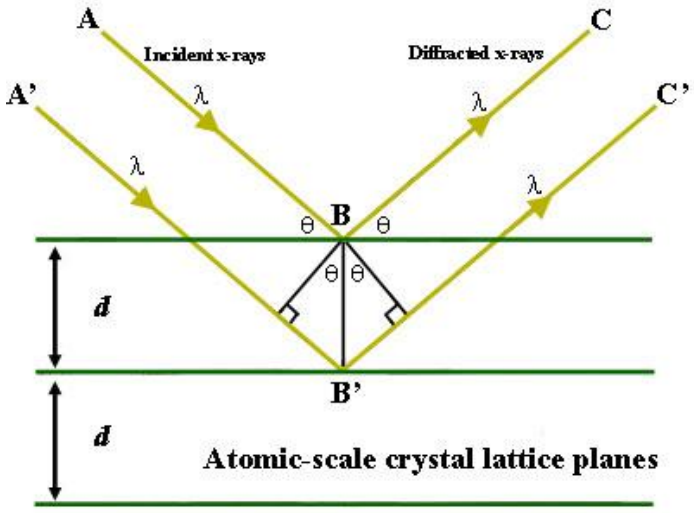

Figure 16: Representation of Bragg's law for diffraction (29)

2.4.2 X-ray goniometer

The X-ray goniometer is a part of the XRD device that moves the detector and the X-ray tube. The rest of the system in an XRD device used for texture measurements consists of a sample holder, the detection system, high voltage generator, the x-ray tube, and associated gearing that moves all the components of the device (21). The goniometer moves and positions the detector and the x-ray incident beam according to the Bragg angle (2θ). A picture of an XRD diffractometer showing a goniometer with the previously mentioned components can be seen in Figure 17. The incident beam optics are on the left side of the device and the diffracted beam optics on the right side (21). The sample holder is in the middle and it rotates around the phi (ϕ) axis. After one full rotation, the sample holder will be tilted around the psi (ψ) axis.

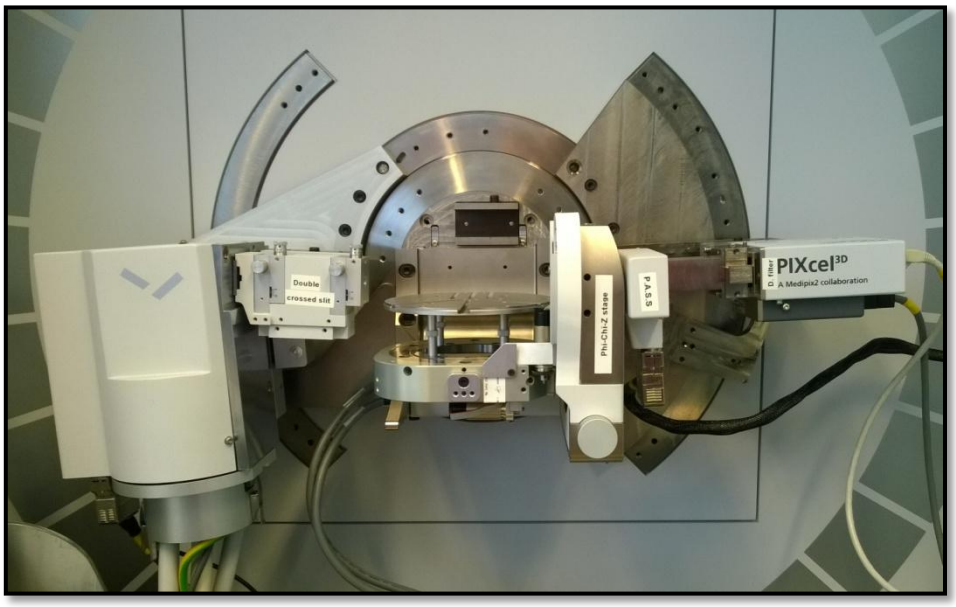

Figure 17: Picture of the XRD diffractometer at Tampere University of Technology

At this point it is relevant to explain in more details the adjustment of the angles on the XRD device, which explains how the X-rays are diffracted towards the detector even when the sample is tilted. One way is known as the Bragg-Brentano focusing condition for reflection geometry. Quite conventional and mostly used, the Bragg-Brentano reflection geometry is based on the parafocusing circles that are shown in Figure 18. In the Figure, S is the source of the x-rays, D the detector, and O the center of the goniometer circle. As can be noticed, all three points lie on the green circle, which is known as the focusing circle. The goniometer circle is represented by the dotted circle and it shows the path around which the detector and the x-ray source move (31). The goniometer circle has a fixed radius *R*, while the radius of the green circle *r*, can be adjusted and changed. It varies from ∞ to R /2, as the angle 2θ varies from 0° to 180°. Because of the geometric properties of the circles, the x-rays that are produced by the source S and

diffracted from any point of the green circle by angle 2θ (from the sample shown in purple color) will arrive at exactly the same spot in the detector D, i.e. $\varphi_1 = \varphi_2 = 180° - 2\theta$ (31).

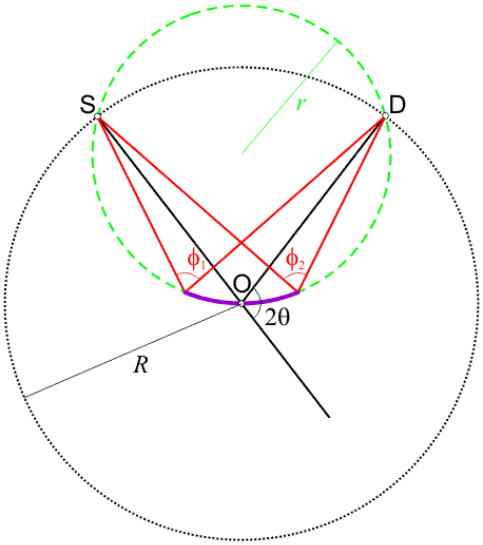

Figure 18: Schematic presentations of Bragg-Brentano parafocusing Circles (31)

Besides Bragg-Brentano there is also a parallel beam geometry, which is the recommended geometry for texture measurements, since with Bragg-Brentano reflection geometry the resulting errors of the measurements are quite high. While in Bragg-Brentano geometry the source-to-detector distance is fixed, parallel geometry allows that the distance can be adjusted. This geometric flexibility enables that the XRD device can be used on a much broader range of sample sizes and shapes. In addition, this geometry is quite insensitive to possible sample displacement errors. Because of these reasons, there is a minimal sample preparation required. Furthermore, parallel beam geometry is recommended for texture measurements of bulk samples (32). Schematic illustration of parallel beam geometry is presented in Figure 19.

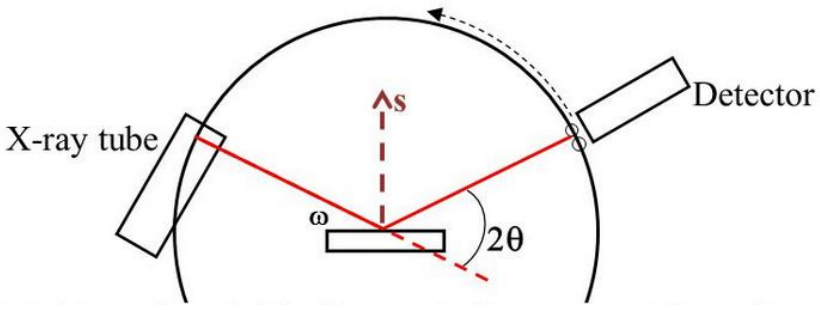

Figure 19: Schematic presentation of parallel beam geometry (33)

2.4.3 Errors in XRD measurements

In XRD, the intensity of the reflected beam will decrease with increasing tilt angle ψ (31). With increasing of the tilting angle (ψ), the intersection of the sample and the incident beam becomes elongated resulting in a defocusing effect (34). This distortion of the projected beam can be observed in Figures 20 a) and b), which show how the elongation changes depending on different Bragg's angles and the tilt (ψ). To get optimum resolution, most x-ray diffractometers today are constructed in such a way that the reflection of the incident beam from an untilted sample (ψ=0) brings the diffracted beam back to the focal point. If the sample is tilted, the effect will be that half of the sample is behind and half is in front of its original plane. For those regions of the sample the focusing condition is no longer true. This results in peak broadening, which is illustrated in Figure 21. Peak broadening will result in a significant drop of the intensity value. Because of this the pole figures should never be measured at $\theta < 10^{\circ}$.

When measuring pole figures using parallel geometry, the defocusing error will be noticed on the outer circles of the pole figure. The inner circles of the pole figure can be measured without any necessary corrections, while the outer parts $\psi > 45^{\circ}$ needs correction. To correct the defocusing the intensities of all ψ angles are normalized (21).

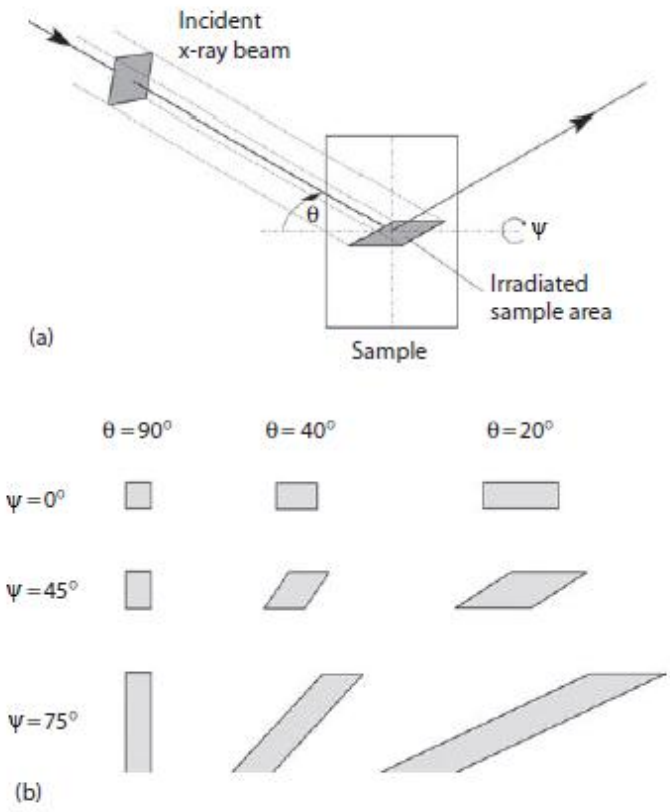

Figure 20: a) A schematic picture of the focus distortion during tilting; b) shapes of the spot at different Bragg and tilt angles (21).

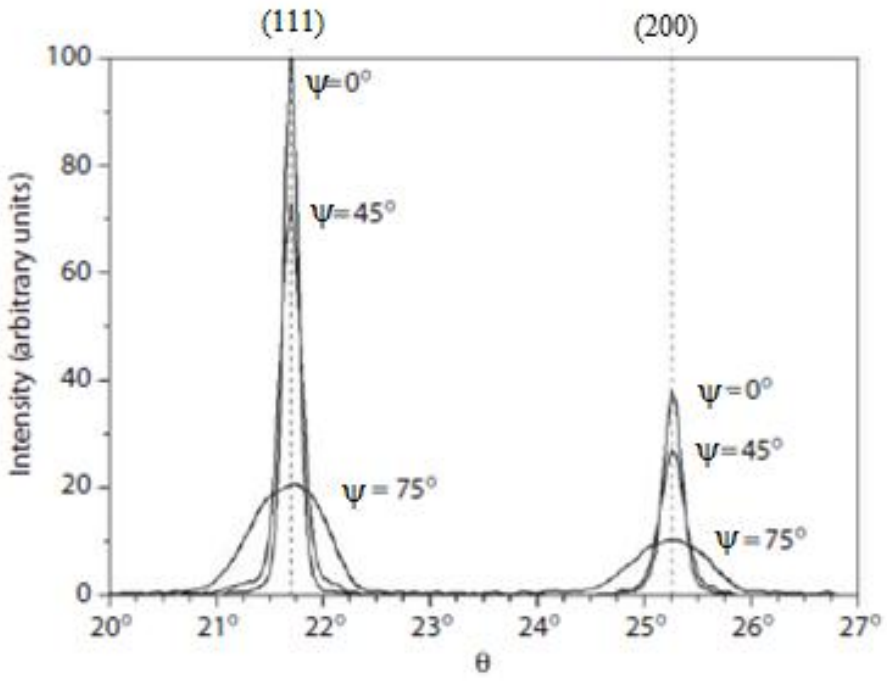

Figure 21: Peak broadening as a result of increasing tilt angle (21).

Besides the defocusing error, absorption of the x-rays and the background error must be considered as well. With increasing sample tilt, the distance that the x-rays travel inside the sample increases. Therefore, there will be a decrease in the diffracted intensity due to higher absorption. However, in the case of thick samples this doesn´t have that much effect as in the case of thin films. Thick samples are usually samples that are thicker than the X-ray penetration depth (around 100 μm). The reason for that is that in thick samples the increase in absorption is balanced by the increased irradiated area (21). The background correction is performed usually at the end of each measurement.

2.4.4 Pole Figure Measurements

In the beginning of a pole figure measurement, the Bragg angle of the *(hkl)* plane is usually determined with a simple quick scan. An example of a quick scan made on textured aluminum is shown in Figure 22.

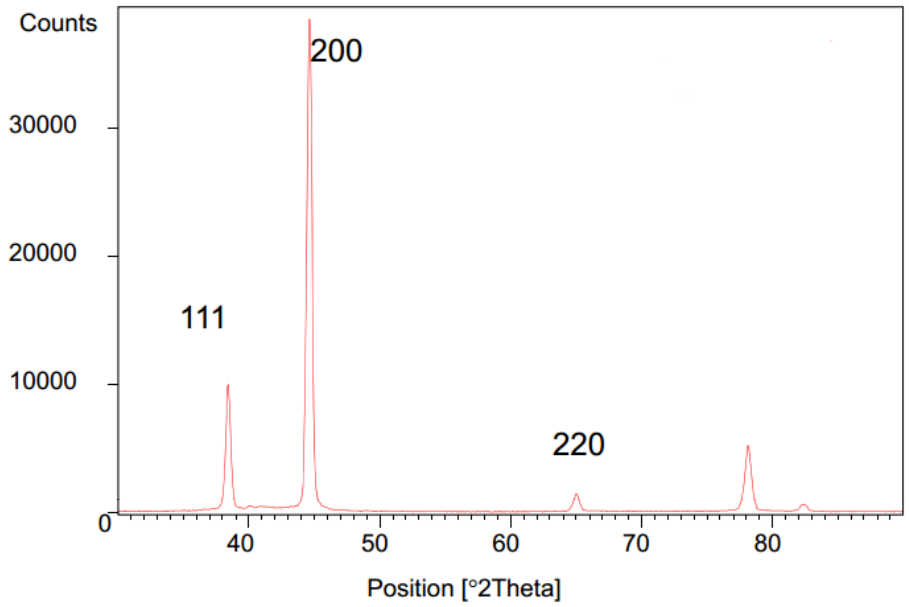

Figure 22: A quick scan of pure aluminum (35).

Figure 22 shows a plot of intensity vs. 2θ angles. After the quick scan is done and the 2θ angles for certain lattice planes are known, the texture measurements can start. It is important to make it clear that the 2θ will be fixed during texture measurements to a certain predetermined value based on the quick scan. When the texture measurement starts, the sample is irradiated with monochromatic radiation at the fixed 2θ angle. Since the diffracted intensity is gained only from the lattice planes that are parallel to the sample surface, in most cases the reflected intensity will be quite week (21). To get the intensities from different sample orientations, the sample is adjusted with different tilting angles and rotated. After the measurement is done, the raw data is processed by the computer software connected to the XRD device and can be presented in a form of a pole figure.

2.4.5 Orientation Distribution Function

Pole figures provide useful information of the material's texture. However, the information is incomplete and more information is needed. The full information is usually gained by crystal orientation distribution function (ODF). The ODF describes the frequency of occurrence of grain orientations in the Euler space (36). It can be presented in a conventional 2-D display in a so called Bunge notation of the Euler´s angles,

as can be seen in Figure 24a), or in a 3D display where all of the three Euler´s angles are shown in orthonormal space, as presented in Figure 24 b) (37).

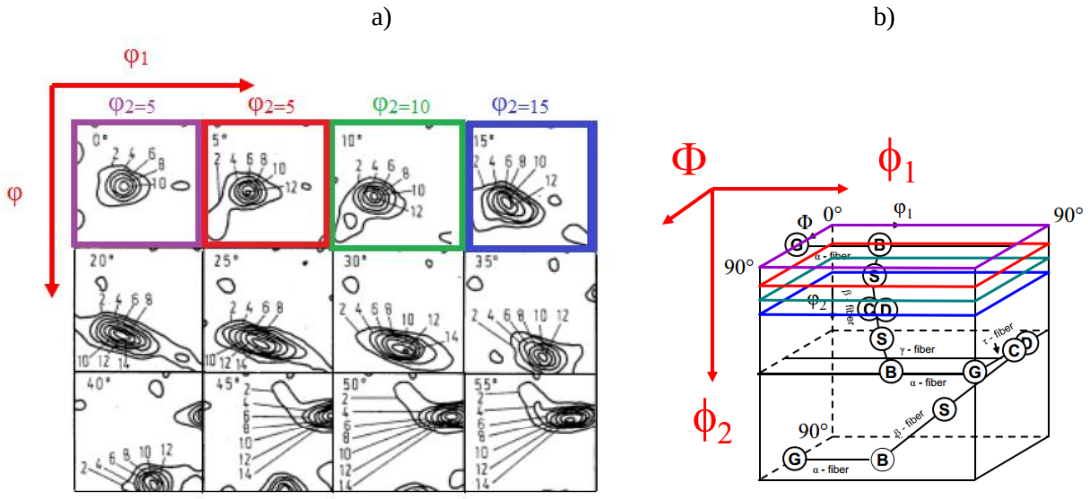

Figure 23: a) 2-D display of the OD sections with fixedφ_2 values; b) a 3-D presentation of the ODF (35).

Through the Bunge notation the ODF is shown as a series of sections where there is one section per a box. Each section shows the variation of the intensity at fixed values of φ_2. The other two angle (φ_1, φ) values change from 0° – 90° as can be better seen in Figure 23 b). By using the ODF images it is much easier to understand the materials texture and to observe the texture fibers.

The ODF images cannot be obtained directly by any technique. There are many different ways how to calculate them. When dealing with texture analysis, a quite commonly used technique is performing a re-calculation of the experimental data gained from the pole figures. There are several mathematical procedures as how to calculate the ODF from the experimental data of pole figures. The most commonly used one is the WIMV method named after Williams-Imhoff-Matthies-Vinel (38). For this way of calculating the ODF, a minimum of three pole figures of different lattice planes are needed. This method uses an algorithm proposed by Williams-Imhoff-Matthies-Vinel in the early 80's. Today, this algorithm is incorporated in almost every XRD software.

2.5 Compression deformation textures

A lot of research today is focused on the principles and development of deformation textures in both industrial and academic sense. It is quite important to understand how the material will behave under certain loads in practical use (39). In our case, the focus of the research is to observe how the texture will change after compression deformation. Under uniaxial compression the texture will be quite different from those developed under tension. In compression the expected result is the rotation of active slip

plane normals towards the compression axis. In tension the active slip plane normals tend to align with the axis of the applied stress (39). In the case of compression of a polycrystalline aggregate, multiple slip will occur and the direction of the lattice rotation will be opposite of that of the tension deformation. In the case of FCC metals, pure materials have different compression texture than the alloys. In pure FCC metals after compression deformation the preferred orientation is a fiber type texture.

In this work the used compression testing method was the Split-Hopkinson pressure bar (SHPB). This type of testing is usually used for testing of the high strain rate materials properties, in this case texture changes during high rate deformation. SHPB provides quite a strong impulse of energy that can be controlled and for that reason is an ideal tool to test materials under dynamic conditions.

2.5.1 Split-Hopkinson bar method

The original idea for the Split-Hopkinson pressure bar method was to measure the stress pulse wave propagation in a metal bar (40). Later on this method was modified by using two bars in series instead of one, today known as Split-Hopkinson pressure bar. This method is used for measuring the stress and strain of the tested material while recording the stress wave propagation in the pressure bars. The method allows various setups and techniques to be applied and can be modified to perform compression, tension, and torsion testing (40).

The underlying principle of the SHPB is the same regardless of the testing that is done. A schematic picture of the SHPB device is shown in Figure 24. The sample is placed between the ends of the two slender bars (between the incident and the transmitted bar) (41). At the end of the incident bar a stress wave is created by impact of the striker bar and the stress wave will propagate through the incident bar towards the specimen. The speed of the striker bar is calculated and provided by a gas gun. Once the wave reaches the specimen it will split into two different waves. One wave will be transmitted and it will propagate through the specimen and into the transmitted bar, while the other one will be reflected and it will propagate away from the specimen back to the incident bar. The cause of the deformation is the difference between the motion of the incident bar and the transmitted bars, assuming that the incident bar moves faster than the transmitted bar. If the sample is very soft, the transmitted pulse can be negligible or even zero although the sample will still deform. Assuming that the caused deformation is uniform across the whole sample, stress and strain can be calculated from the amplitudes of the incident, transmitted and the reflected wave (41). In this method it is important that the bars stay in the elastic region during the testing and that they are properly aligned so that the achieved stress state is uniform.

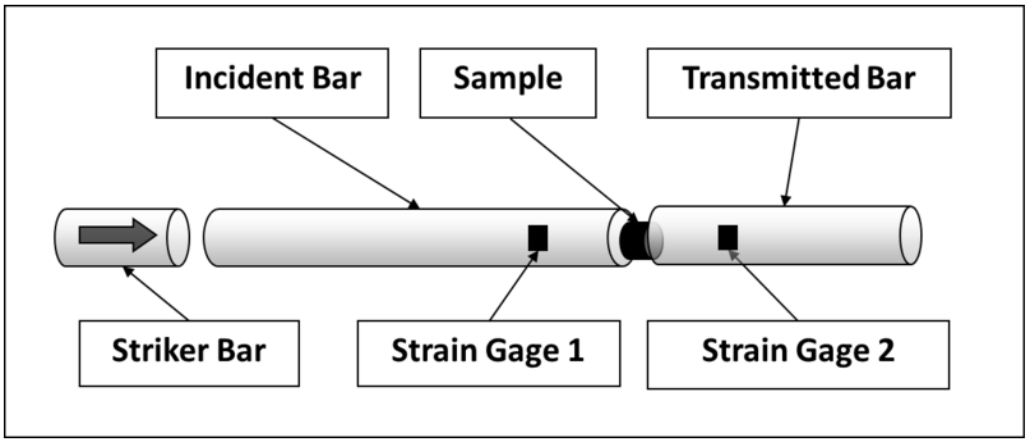

Figure 24: Split Hopkinson pressure bar setup (42)

3. EXPERIMENTAL PART

3.1 Procedures and materials used in the testing

The aim of this research was to determine the effect of high rate axial deformation imposed on pure aluminum that had been ECAP processed. The texture of the samples was characterized using XRD. After that additional axial compression deformation was introduced to the samples using the Split Hopkinson bar device. The texture was then re-measured.

3.1.1 Samples and preparation

As already mentioned the samples were commercially pure aluminum that had been pressed through the ECAP dies for one, four, or sixteen times. The samples were circular cross-section billets and the routes of the ECAP are not known. The dimensions of the samples are shown in Table 2.

Table 2: Dimensions of the tested samples.

Sample	**l** (mm)	**d** (mm)
ECAP 1	6.76	9.65
ECAP 4	9.88	9.58
ECAP 16	9.66	9.65

The samples were cut from the original ECAP'ed bar in such a way that the surface of the samples was perpendicular in respect to the length of the samples. The surfaces of the samples were quite straight and flat. Therefore, the sample preparation consisted of only finishing the sample surfaces by mechanical polishing. This was done with fine silicon carbide abrasive paper, after which the SiC paper was changed for a fabric pad or so called napless cloth for final polishing. This is done by adding slurry of diamond onto the cloth to produce a mirror like surface (scratch free).

In practice the sample preparation does not have to be this strict. It is enough that the sample is cut in such a way that the surface is flat and is perpendicular to the sides of the sample. In this thesis one set of XRD measurements were performed before the samples were mechanically polished and then repeated after polishing. This was done in order to see if there are any significant changes in the results depending on the final polishing of the samples.

3.1.2 Equipment and test procedures

Texture measurements were done with PANalytical Empyrean XRD device, which is a multipurpose diffractometer. The setup used for the purpose of this thesis can be divided to the hardware setup and software setup. The hardware setup consists of the X-ray tube, sample holder, incident beam optics and diffracted beam optics. The used components in the hardware setup are listed in Table 3.

Table 3: List of hardware setup components

Hardware setup	Hardware components
X-ray tube	-must be configured to point focus
Incident beam optics	-X-ray tube and double crossed slits collimator
Diffracted beam optics	- P.A.S.S. and D. filter
Sample holder	- Phi-Chi-Z stage

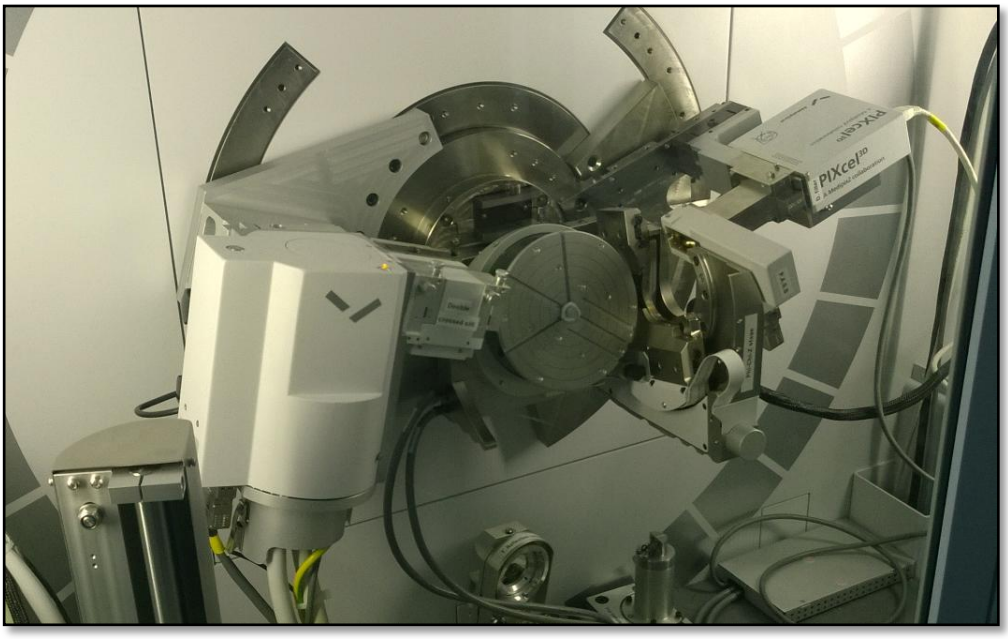

Figure 25: PANalytical XRD device for texture measurements at Tampere University of Technology.

After the hardware setup, the hardware information is updated on the Data Collector software and the optics setup is done. Tables 4 and 5 summarize the incident and diffracted beam optics used in the measurements.

Table 4: Incident beam optics software setup

Incident Beam Optics	Setup Options
Prefix module	- cross slits collimator
Divergence slit	- cross slit height 2 mm
Anti-Scatter slit	- none
Mask	- cross slit width 2 mm
Mirror	- none
Monochromator	- none
Beam Attenuator	- none
Filter	- none
Soller slit	- none

Table 5: Diffracted beam optics software setup

Diffracted Beam Optics	Setup Options
Prefix module	- parallel plate collimator 0.27˚
Anti-Scatter slit	- programmable anti-scatter slit
Receiving slit	- OD
Collimator	- coll. 0.27˚
Detector	- PIXcel3D detector [1] - Type: detector [1] - Lower level:35,0% - Upper level: 85,0% - Used wavelength: K-alpha
Mask	- none
Mirror	- none
Monochromator	- none
Beam Attenuator	- none
Filter	- large Beta-fi Nickel
Soller slit	- large 0,04 rad

When both hardware and software setups are completed, the sample is mounted in the centre of the Chi-Phi-Z sample holder, as can be seen in Figure 25. At this point the height of the sample must be adjusted in order to ensure that the x-rays do not miss the sample during the measurement. The final step before the actual texture measurements is to perform a quick scan of the sample to find the 2θ values of the lattice planes as explained previously. Figure 26 presents the results of the quick scan from the samples used in this thesis.

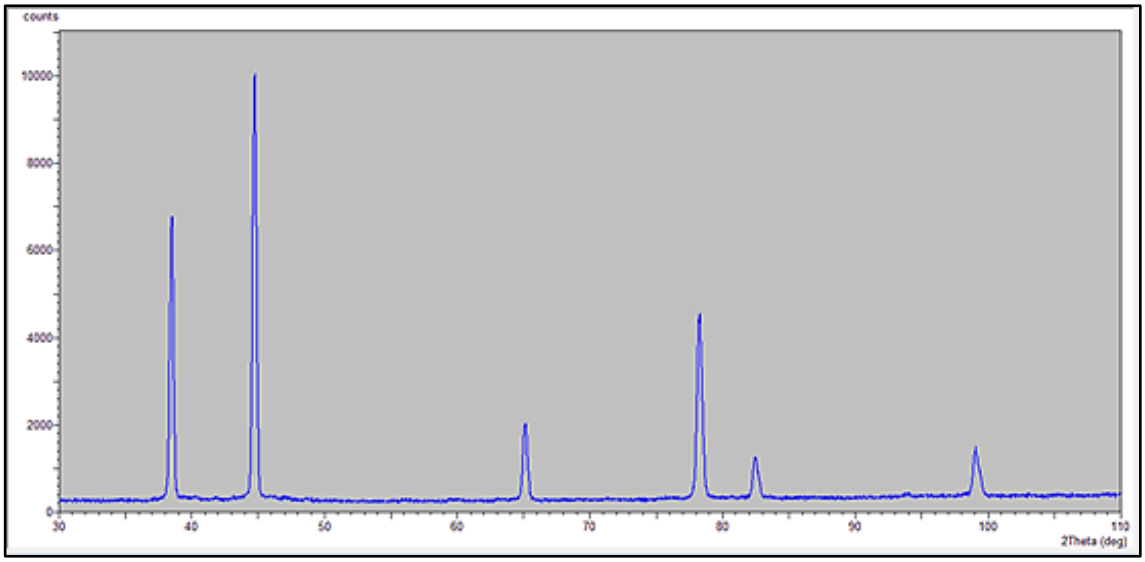

Figure 26: Quick scan of single ECAP pass pure aluminium sample

The first peak for the (111) lattice planes is at 38,4700 degrees, the second peak for the (200) lattice planes at 44,7250 degrees, and the third peak for the (220) lattice planes at 65,1330 degrees. These values were used for all three samples (ECAP_1, ECAP_4 and ECAP_16). The quick scan was performed for all three samples just once before the first set of measurements.

The compression testing was done by the SHPB method using the device built at Tampere University of Technology presented in Figure 27. This SHPB device uses three high strength maraging steel bars of yield strength ~ 1900 MPa. The diameter of the bars is 22 mm and their length is 1200 or 1800 mm. The striker bar is of the same material as the other bars and of the same diameter but of different length (between 200 and 400 mm). Each bar in the device setup is supported by 3 bearings at four different stanchions. These bearings can be moved in x and y directions in order to align the bars before the testing. Behind the striker bar is a gas gun that consists of a barrel, a pressure container, and a vacuum system used to reload the striker bar. For measuring the velocity of the striker bar there are three optical IR-sensors. There are also two strain gauges positioned in the middle of the incident and transmitted bars. The strain gage signals from the bars are amplified using Kyowa CDV 700A series signal conditioner and recorded on a12-bit 10M Sample Yokogawa digital oscilloscope. The SHPB device is fully operated by a computer, including the loading of the striker, pressurizing the pressure vessel, shooting, and finally downloading the data from the oscilloscope for further analysis (43).

Figure 27: Compression SHPB device setup at Tampere University of Technology.

The test conditions used in this thesis were room temperature, striker length of 300 mm, striker speed of 10 m/s, launching pressure of 1,3 bars and the aimed strain rate of 1000 1/s. The same conditions were used for all 3 samples. After the measurements were done, the stress, strain, and strain rate in the sample were reduced from the raw data (the elastic stress pulses in the bars) using Matlab codes developed for the purpose.

4. Effect of different variables on texture measurements

4.1 2θ angle effect on the measurement results

In this chapter the focus of the study is the effect of 2θ angle on the accuracy of the texture measurement results. Figure 28 shows three pole figures that were measured from the same sample (ECAP_1). The observed lattice plane was (111) in all three cases.

a)

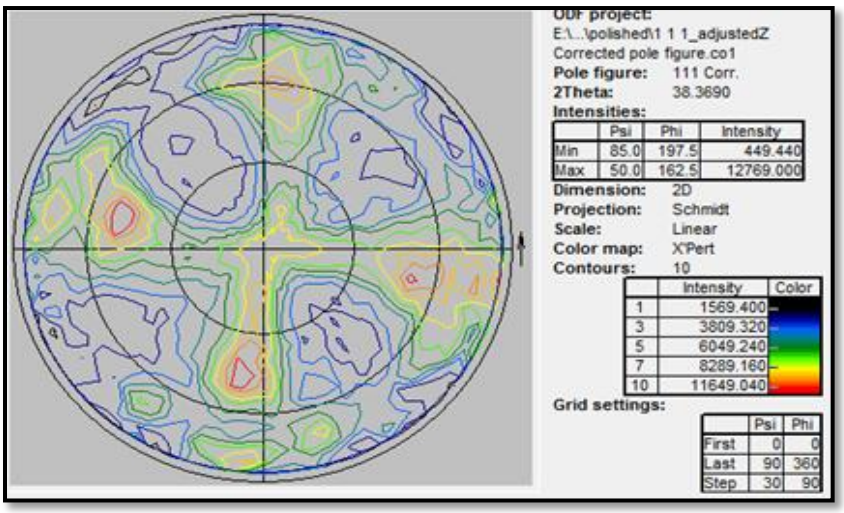

b)

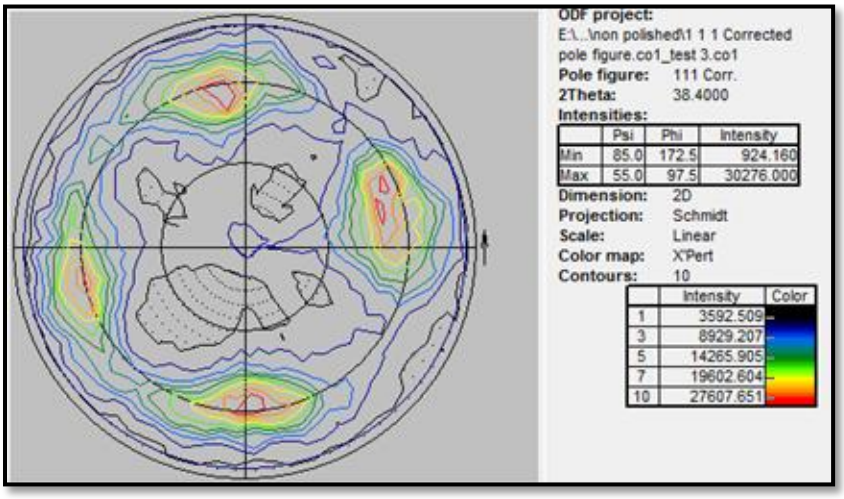

c)

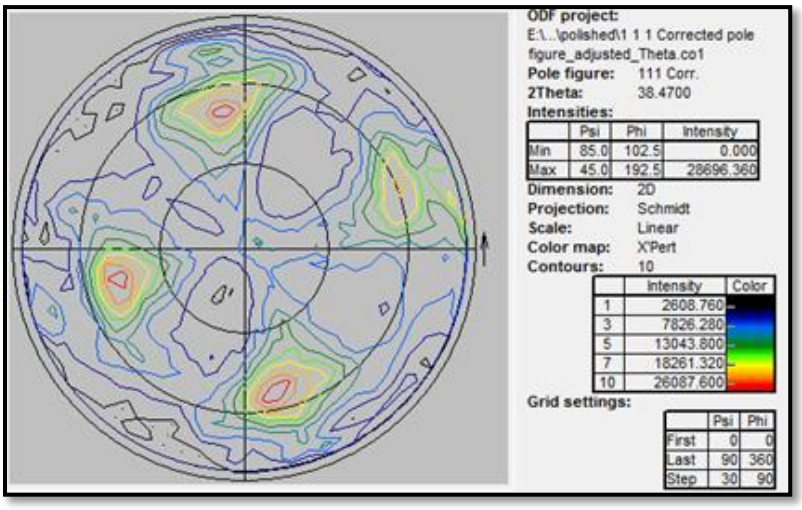

Figure 28: (111) pole figures of an ECAP_1 sample taken under different 2θ angles.

Before the texture measurements, a quick scan was performed to determine the exact value of the 2θ angle for every lattice plane that would be measured. These angels are already well known in the literature for pure materials. In the International Centre for Diffraction Data (ICDD) there is a selection of standard cards with all lattice plane angles for most materials. These ICDD standard cards are quite useful for cross-checking the resulting 2θ angle values. However it is still recommended to perform the quick scan for each sample to get the exact values. In Figure 28 the three pole figures were scanned from the same sample just with different 2θ angles. The sample was removed from the XRD device between the measurements and was not positioned back properly at this point. That is the reason why it looks as if there is a rotational symmetry between Figure 28 a) and the Figures 28 b) and c). However, in reality there is not any rotational symmetry and in all three images the texture clusters are in the same positions. Figure 28 a) has the 2θ angle value of 38.3690, and is significantly different from that in the other two pole figures. The texture clusters are not as clear and but quite diffused. In Figure 28b) the 2θ angle is 38.400, and the pole figure shows four clear intensity clusters. The Figure shows a clear 2-fold symmetry and good intensity values. The last image in Figure 28 c) has the 2θ angle according to the resulting quick scan of our measurements, i.e., 38.4700. It shows four intensity clusters and gives information on the texture around the clusters in a less confusing way than Figure 28 a). In conclusion, since the results of the scans vary with small differences in the 2θ values, the 2θ angles must be properly adjusted for each specimen.

4.2 Effect of the defocusing error

Since all the measurements in this thesis were done in parallel beam geometry, the results have a certain amount of defocusing error. The intensity of the defocusing error will increase with higher tilting angle (ψ) during the measurements, and as a result there will be a significant intensity drop in the results. The intensity drop will depend on the alignment of the sample and the goniometer of the XRD device, the size of the collimator and on the receiving slits. The smaller the collimator and the larger the receiving slits are, the smaller is the defocusing error.

a)

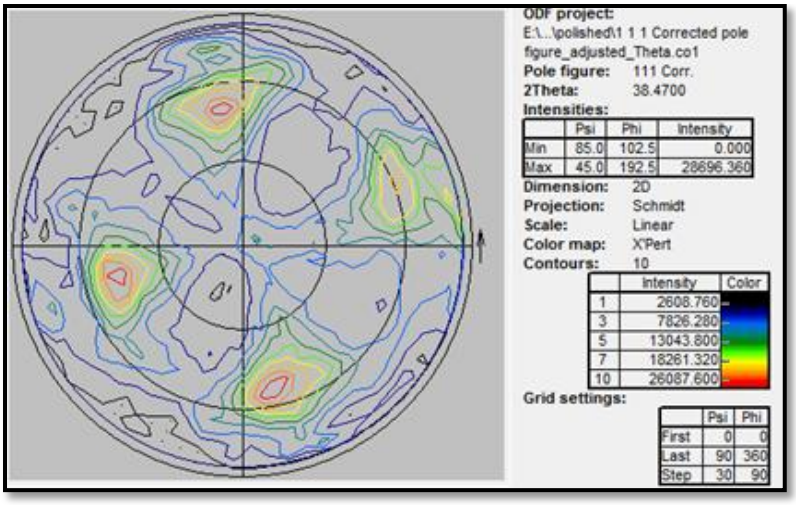

b)

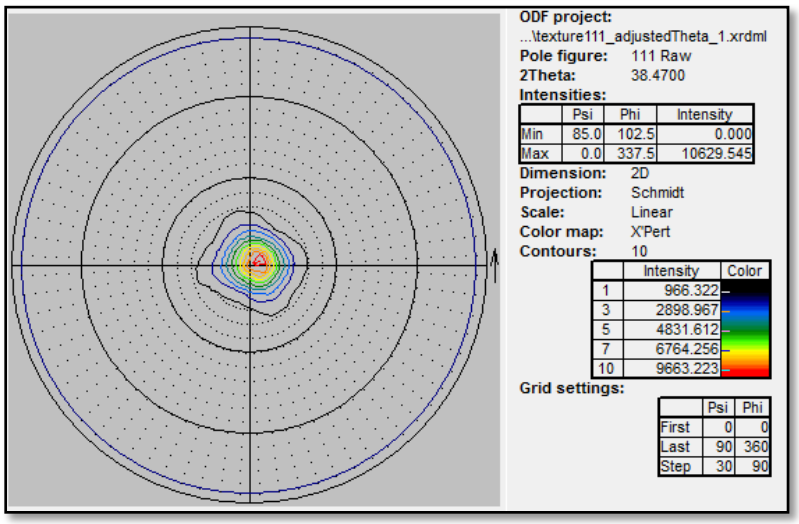

Figure 29: (111) pole figures from ECAP_1 sample, a) corrected; b) before correction.

In our case the receiving slits were not fully open and the defocusing error was large, as can be noticed in Figure 29 b). However, the correction is rather simple to perform so in the end the adjustment of the receiving slits was not so significant. In Figure 29 b), which shows the raw image without any corrections, the defocusing error will have the biggest effect on the outer circles of the pole figure . All the data is in the inner circle area (ψ< 45°) and the pole figure cannot be used in this form. Figure 29 a) shows

the result after the correction function was applied. The correction function normalizes the intensity for any value of ψ angle.

4.3 Effect of sample preparation

As described in Chapter 3.1.1, the samples were cut such a way that the surface was perpendicular in respect to the sides of the sample and mechanically polished. Figures 30a) and b) show the measurement results from the same sample measured before and after the additional mechanical polishing, in that order. The resulting figures show no significant difference except in the intensity values presented in the legend of both pole figures.

a)

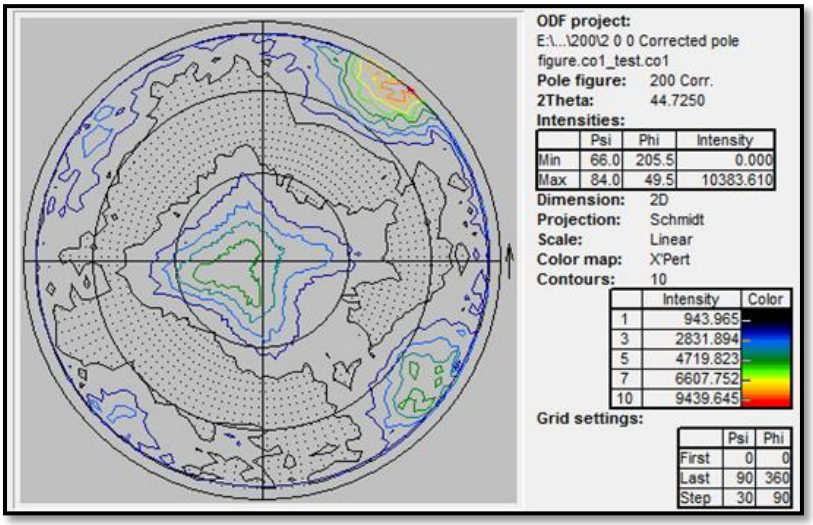

b)

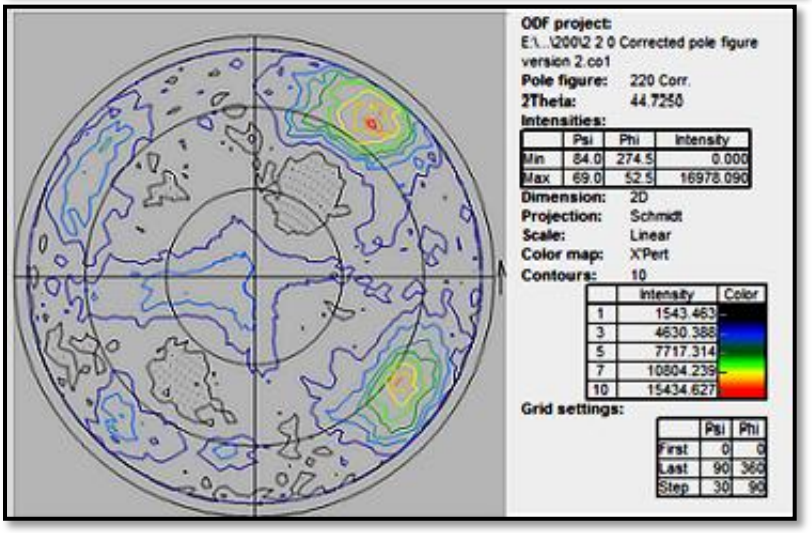

Figure 30: (220) pole figures from ECAP_1 sample, a) before additional polishing, and b) after mechanical polishing.

The pole figure in Figure 30a), which was measured before polishing, shows five visible intensity clusters. One cluster has a maximum intensity, two are a bit weaker (marked in green color), and the last two are hardly visible (marked in blue color). In

The pole figure in Figure 30b), which was taken with the same 2θ angle as that in Figure 30 a) contains also five texture intensities in the exact same positions. It can be noticed that the intensity values obtained after polishing the sample are almost doubled even though the pole figure itself does not look significantly different. Two of the texture intensities show maximum intensities, while the other three are a bit weaker (marked in blue). The reason for these small intensity differences could simply be due to the fact that during the mechanical polishing a small layer of the sample was removed from the surface. As a result the sample was not irradiated at the exact same spot as it was before polishing. However, these differences are so small that they can be concluded irrelevant. If the sample does not have cracks or scratches on the surface and it is cut in such a way that the surface of the sample is parallel to the sample holder, no additional polishing is needed.

5. Compression deformation by Split-Hopkinson bar method

The compression test results are presented in the following figures. There are two different plots for samples ECAP_1, ECAP_4 and ECAP_16 i.e., true stress v. true strain and strain rate vs. time. The true stress vs. true strain curves for all three samples were plotted in the same figure for easier analysis, and it shows that there is a significant difference between them and the curves follow almost the same pattern. However, the yield behaviour of the samples is a bit different. Sample ECAP_16 presented in Figure 31 with black color shows lower yield strength in comparison to sample ECAP_4 presented with red color. The reason for that is most likely that the sides of the ECAP_16 sample were not as parallel as in the other two samples.

The results of the SHPB are not the main focus of this thesis and therefore will not be further analyzed. The most important aim here was to perform the testing correctly and to create additional deformation in the ECAP'ed samples.

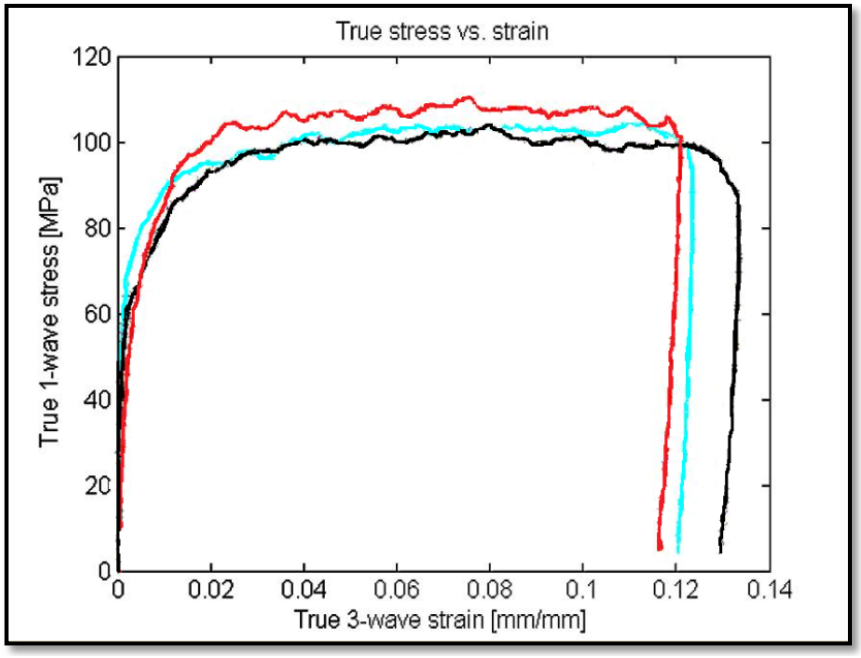

Figure 31: True stress vs. strain plot for ECAP_1 (blue line), ECAP_4 (red line), and ECAP_16 (black line).

ECAP_1:

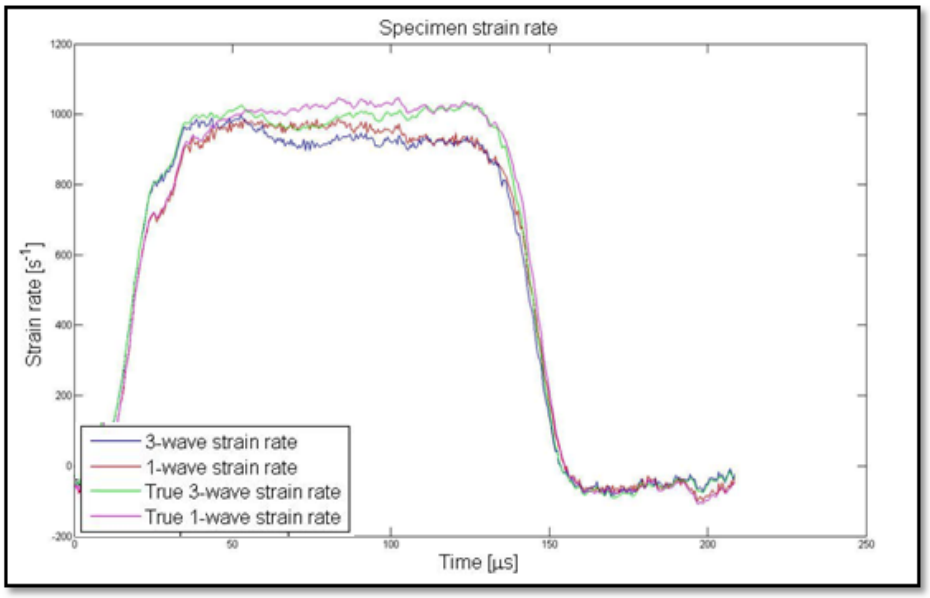

Figure 32: Strain rate vs. time plot for ECAP_1 sample.

ECAP_4:

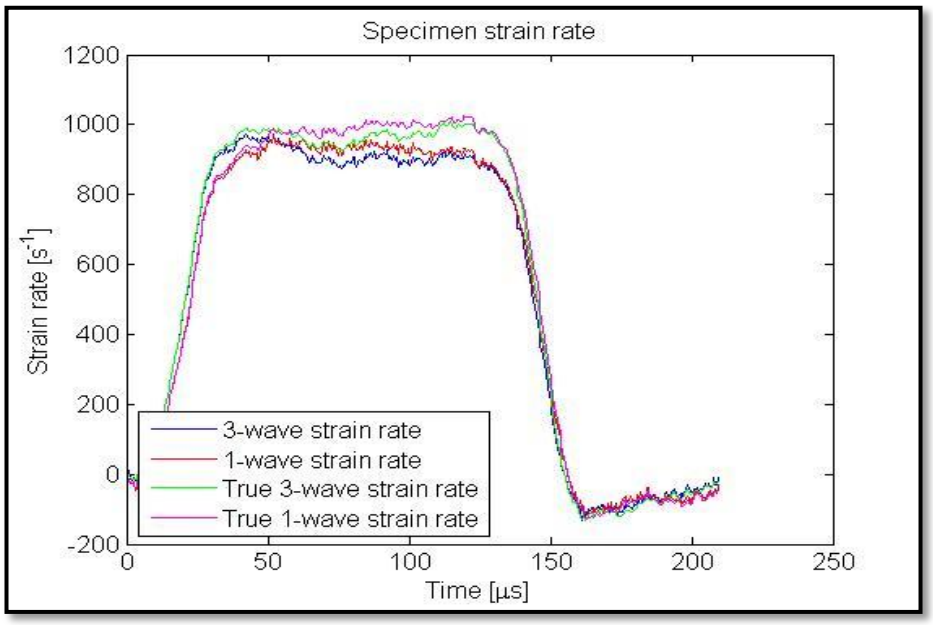

Figure 33: Strain rate vs. time plot for ECAP_4 sample.

ECAP_16:

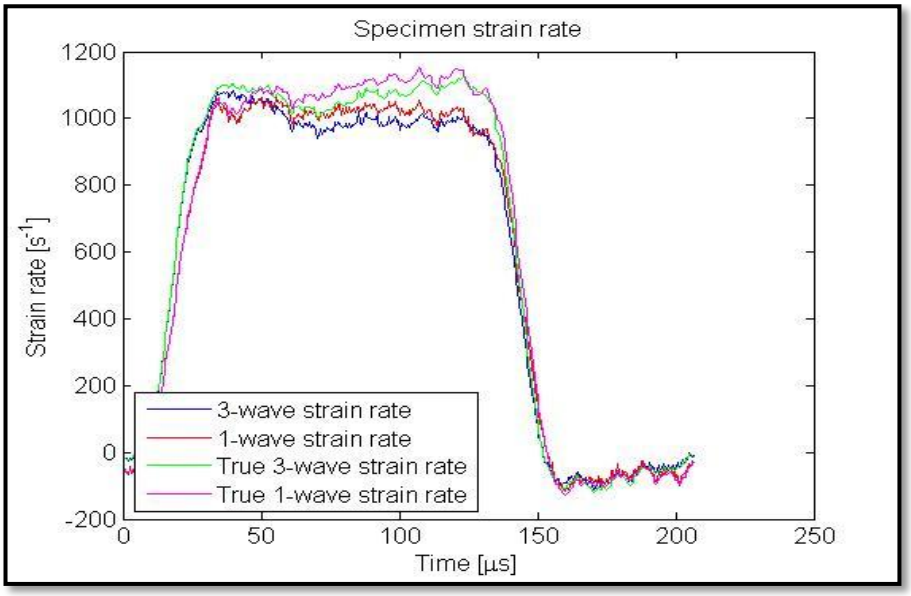

Figure 34: Strain rate vs. time plot for ECAP_16 sample.

6. Results and Discussion

The detailed results for ECAP_1 sample are presented in Figure 47 (Appendix 1) for the lattice planes (111), (200), and (220). The results match the literature results, which state that the developed texture in FCC materials after just one ECAP pass can be compared to the texture of simple shear deformation with the 45° tilt around the ED axis. These ECAP_1 results are also presented in a combined Figure 35 for easier comparison. The red marked points indicate the positions of the intensity clusters in ideal simple shear deformation of the mentioned lattice planes, presented in the form of pole figures.

Since it is not known with which route our samples were processed or how were the axes defined (which axis would be the TD and ND), it s a bit unclear in which direction the shear deformation has occurred. According to the literature (25), in FCC materials there are commonly lattice rotations where the (111) plane has a strong tendency to align with the shear plane and/or where the <110> slip direction aligns in the direction of shear in all processing routes. However, this cannot be determined for these samples since they were measured from the front face part. If they were cut in such a way that the side of the samples could be measured, it would be possible to estimate also the shear direction.

a) (111) b) (200) c) (220)

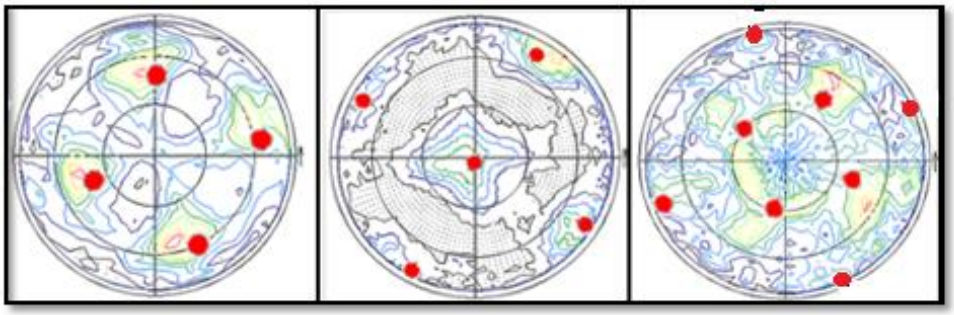

Figure 35: Pole figures of ECAP_1 sample and FCC material in ideal shear deformation (marked with red dots).

By comparing the results from the ECAP_1 sample with the ideal shear deformation (Figure 35a) for (111) lattice plane it is easy to see that the resulting pole figures shows the same four intensity clusters, a 2-fold symmetry and a 45° tilt around the ED axis. In the case of (111) pole figure the clusters should be positioned in such a way that there is a 90° angle between them. In Figure 35 b) which presents the resulting pole figure for the (200) lattice plane, there are five intensity clusters, as in the case of ideal shear deformation (Figure 35 b) marked in red). If we compare the resulting pole figures of (111) and (200) planes (Figure 35a) and b), it is easy to see that the clusters of (200) pole figure would be positioned approximately between the ones in the (111)

pole figure. Similarly to the (111) pole figure, also the (200) pole figure shows a clear 2-fold symmetry. The third lattice plane in the ECAP_1 sample is (220), which shows five prominent intensity clusters (Figure 35 b). There are two quite clear intensity clusters with high intensities while the other three are of a bit lower intensities. In Figure 35 b), (marked with red) there are eight intensity clusters only because this is a presentation of an ideal result. In the resulting pole figure tree of the intensity clusters that would be positioned close to the edges of the pole figure are not visible. This is because of the size of the scanning area that was probably small.

The resulting images for ECAP_4 sample are presented in detail in Appendix 1 (Figure 48). For easier discussion, Figure 36 is presented with combined results of ECAP_4 sample. ECAP_4 sample results show slight changes in the texture development from those after just one ECAP pass. In the (111) lattice plane pole figure (Figure 36a), there are still four prominent intensity clusters. However, in comparison to the (111) pole figure of the ECAP_1 sample, the ECAP_4 (111) pole figure looks a bit more diffused and the intensity clusters are less clear, even though the intensity counts are much higher for the (111) lattice plane in ECAP_4 sample. Furthermore, when comparing ECAP_1 and ECAP_4 pole figures, there appears to be a presence of a rotational symmetry. However, since the axes of the samples were not initially defined, we cannot be sure if there is really a rotational symmetry or is the sample just placed in the XRD device in that way. According to the literature, there should be a clear rotational symmetry. The values of texture intensities in the pole figures of (220) and (200) lattice planes (Figure 48 b and c) are a bit lower than in ECAP_1 for the same plane, and are not as clear as the previous ones. There is a clear presence of both α and β fibers which is visible because the intensity clusters are concentrated around the fibers and have the highest intensities where the fibers cross each other. That can be noticed especially in the (111) pole figure for ECAP_4 sample (Figure 36 a). α fibers are marked with red lines and β fibers with green lines in Figure 36.

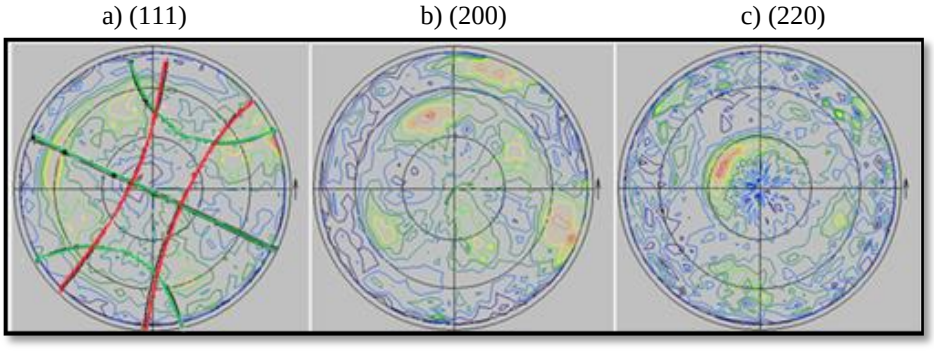

Figure 36: Combined results of ECAP_4 sample

The results of ECAP_16 sample, (Figure 49 of Appendix 1 shows the detailed results) presented in Figure 37 show that the resulting pole figures are even more diffused and that it is more difficult to clearly see the intensity clusters than before. For the (111) lattice plane it is still possible to see four prominent intensity clusters even though they spread out significantly compared to ECAP_1 and ECAP_4 samples. For the other

two lattice planes the resulting figures are quite hard to analyze because it is not completely clear where the highest intensities are. This is especially the case for the (200) lattice plane (Figure 37 b) where the intensity clusters cover almost the whole middle circle area of the pole figure. Again the highest intensities of the clusters are in the areas where the α and β fibers are crossing each other. Compared to ECAP_1 and ECAP_4 samples, ECAP_16 has the lowest intensity values.

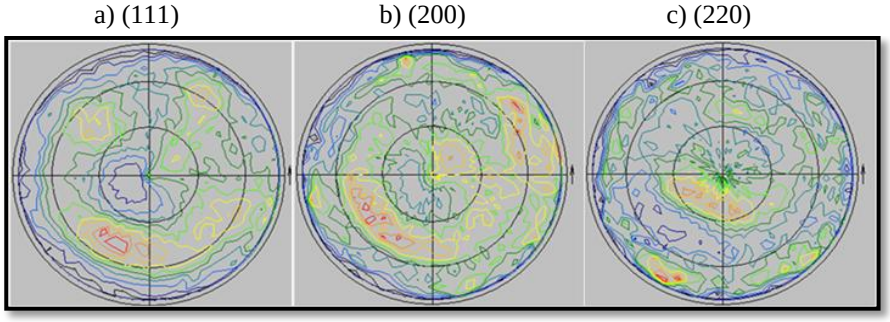

Figure 37: Combined results of ECAP_16 sample

After the SHPB compression deformation the ECAP_1 sample results (Figure 50 of Appendix 2) indicate that the developed texture is not too different from that before the test. The results are also presented in Figure 38. There are still all four intensity clusters visible but with significantly higher values of intensities compared to those before compression. Besides the higher intensities there is no significant difference between the initial texture and the one after the compression deformation of ECAP_1 sample. Since the samples were marked before the first XRD measurements so that they can be positioned in the exactly the same position in the second measurement, the results can be directly compared to the samples before the SHPB compression deformation when it comes to the rotational symmetry. According to the literature in compression deformation the active slip plane normals will rotate towards the compression axis. This can be noticed for all three samples, as well as that the rotation increases with the higher number of ECAP passes. Furthermore, in all three pole figures there is a clear 2-fold symmetry, and it can be noticed that there are almost no intensities visible in the middle of the pole figure. For the (220) and (200) pole figures presented in Figures 38 b) and c), we can notice a significant difference in comparison to the initial texture. The intensity clusters are very weak in the center area of both figures and stretch in the rotation direction towards the compression axis.

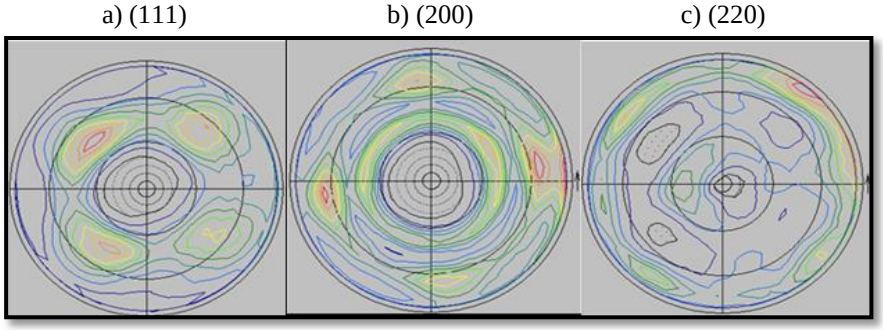

Figure 38: Combined results of ECAP_1

The results for ECAP_4 sample show quite a significant difference compared to the initial texture results. Complete results are presented in Figure 51 (Appendix 2), while Figure 39 is used for easier visualization. In the (111) pole figure there are still four clear, prominent intensity clusters and a visible rotational symmetry compared to the initial results (Figure 39a). In the other two pole figures (220) and (200), the intensity clusters are spread out and quite diffused (Figures 39 b) and c). It shows that the intensity clusters around the main texture fibers are slightly weaker compared to ECAP_1 sample. However, the intensity values of ECAP_4 sample are significantly higher than for ECAP_1 in all three pole figure images. It is still clear that there are both α and β fibers present and that the highest concentrations of the intensity clusters are around the intersections of the fibers. This can be best observed in the (111) pole figure (Figure 39 a). This would indicate that after four ECAP passes the material got even stronger than after just one. This can be backed up with the compression deformation results presented in Figure 31, where it is clear that ECAP_4 has a higher yield strength.

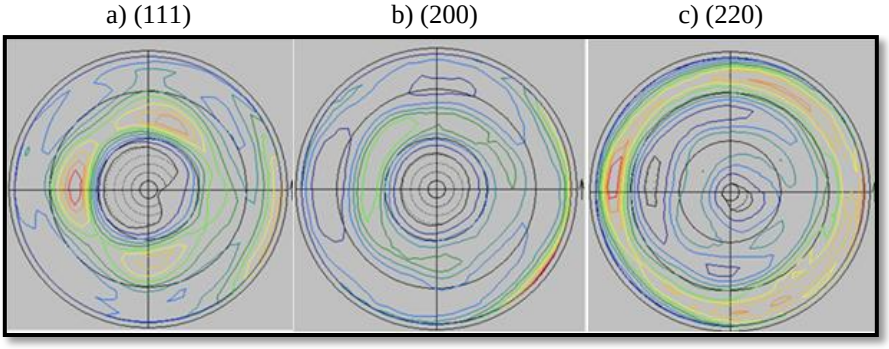

Figure 39: Combined results of ECAP_4

The results for ECAP_16 sample are presented in Figure 52 (Appendix 2) and Figure 40. They show that the material is slightly losing its strength and becoming softer (this is also supported by the compression deformation results in Figure 31). The textures presented in Figures 52 a), b) and c) are presented in a linear scale. Since the resulting images are quite difficult to analyze, the same images are presented in the logarithmic scale in Figures 53 and 40. There it can be noticed that the texture is diffused and that all intensity clusters have moved around the edge of the pole figure circle. This is supported by the literature (44), (45) which suggests that with more ECAP passes the intensity clusters weakens around the texture fibers.

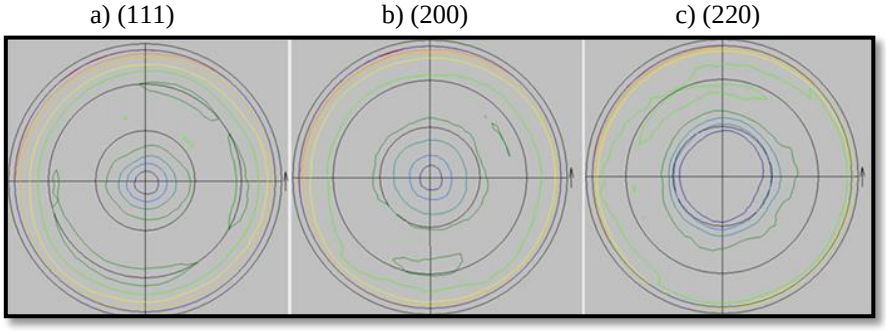

Figure 40: Combined results of ECAP_16

The following Figures (41 thru 46) show the OD results for φ_2= 0° and 45° values corresponding to the pole figures of ECAP_1, 4 and 16 samples. For easier comparison the results before and after deformation ODFs are presented for all three samples. Textures of the samples before compression deformation (Figures 41, 43 and 45) show that for ECAP_1 sample the texture is quite inhomogeneous. This gradually changes towards homogeneous texture with increased number of ECAP passes. This can also be observed in the 3-D presentation of the results in Figures 54, 56 and 58. ECAP_1 sample has texture that is close to the ideal shear texture, while in ECAP_4 and 16 there is a significant deviation from the ideal shear texture. By comparing the texture before and after the compression deformation in Figures 41 and 42 for sample ECAP_1, it can be noticed that the texture fibers have shifted by about 45° along the φ_1 axis. This corresponds with the rotational symmetry between these two samples.

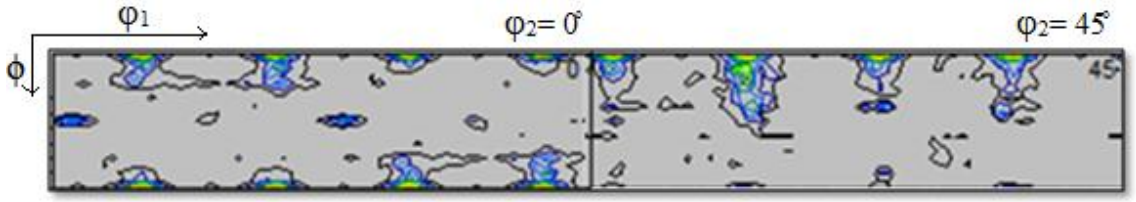

Figure 41: OD (0° and 45°) of ECAP_1 sample before compression

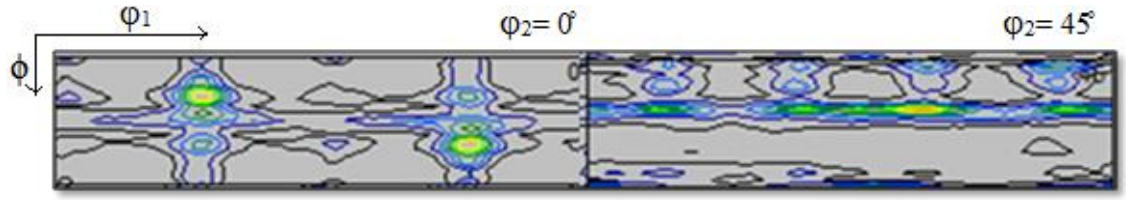

Figure 42: OD (0° and 45°) of ECAP_1sample after compression

Texture development of sample ECAP_4 shows a weaker texture compared to sample ECAP_1 in both before and after compression deformation cases. The 3-D presentation of ODF (Figure 56) shows higher concentration of texture components that are much smaller than in ECAP_1. Also the intensity levels are higher than in results for ECAP_1 before compression deformation. Furthermore, in Figure 43 it is noticeable how the texture gets more diffused, which corresponds to the pole figure analysis. After compression deformation (Figure 47) the components form elongated shapes along the φ_1 axis. In the OD Figures (43 and 44) for the φ_2 =45°, the presence of rotational symmetry is evident because there is again a shift along the φ_1 axis.

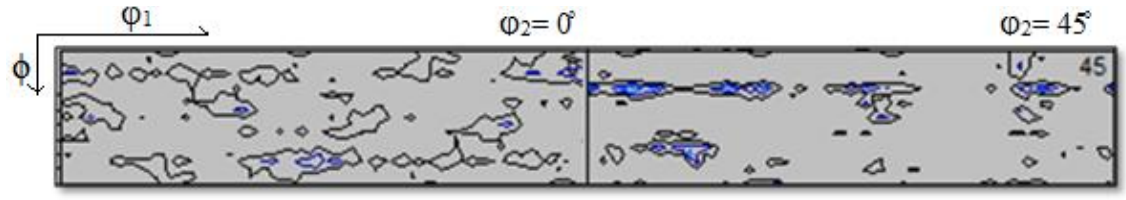

Figure 43: OD (0° and 45°) of ECAP_4 sample before compression

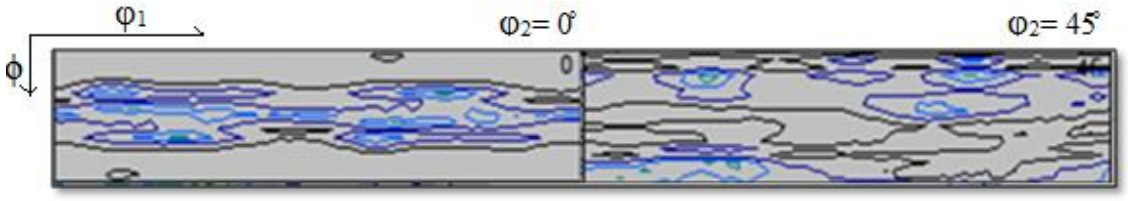

Figure 44: OD (0° and 45°) of ECAP_4 sample after compression

ECAP_16 sample before compression deformation (Figure 45) shows an even more diffused texture and higher component concentrations around the fibers. The results after the compression deformation are quite difficult to analyze. The texture components after compression deformation are fully elongated along the whole φ_1 axis and parallel with respect to each other (Figure 46). The texture is significantly weaker and so are the intensity levels, too. As in the pole figure analysis it is not possible to determine if there is a rotational symmetry between the results before and after the deformation.

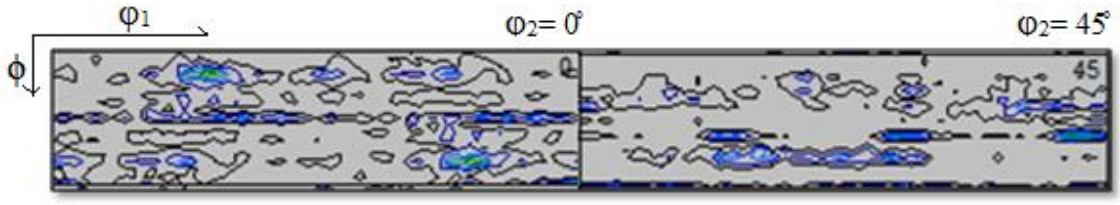

Figure 45: OD (0° and 45°) of ECAP_16 sample before compression

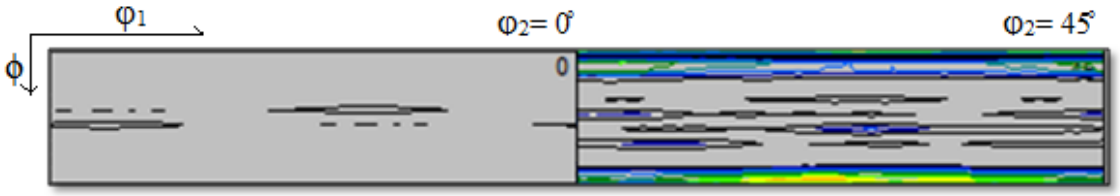

Figure 46: OD (0° and 45°) of ECAP_16 sample after compression

7. SUMMARY

The following conclusions can be summarized from the presented results and the discussion part of this thesis. All conclusions are supported by the studied literature:

1. The texture development of pure aluminum after one ECAP pass can be directly compared with the texture of simple shear deformation.
2. There is a 2-fold symmetry present in all pole figures for samples that were ECAP processed one and four times.
3. Presence of rotational symmetry for ECAP_1 and ECAP_4 samples when comparing the results before and after the compression deformation. For ECAP_16 sample the presence of rotational symmetry was not possible to determine.
4. Texture in ECAP_1 is inhomogeneous shear texture, which will change towards homogeneous texture with increasing the number of ECAP passes.
5. With increasing number of ECAP passes the intensity clusters will concentrate more around the texture fibres.
6. After additional compression deformation the intensity clusters will move away from the texture fibres, the texture becomes weaker and more spread towards the edges of the pole figures. This increases with higher number of ECAP passes.
7. Compression deformation will affect the texture in such a way that the intensity clusters rotate towards the compression direction axis. This also increases with higher number of ECAP passes
8. 2θ angle has a significant effect on the accuracy of the results and must be adjusted properly
9. Defocusing error also has a significant effect on the results. However it is rather simple to perform the correction.
10. If the sample is cut in such a way that it contains no cracks, scratches and is parallel with the sample holder, no additional polishing is needed.

APPENDIX 1

Initial texture measurements of the ECAP'ed samples

The results presented here were measured with 45kV voltage and 40mA current in a continuous scan mode. Both background and defocusing measurements were performed and the errors have been removed from the images below.

ECAP_1:

a)

(111)

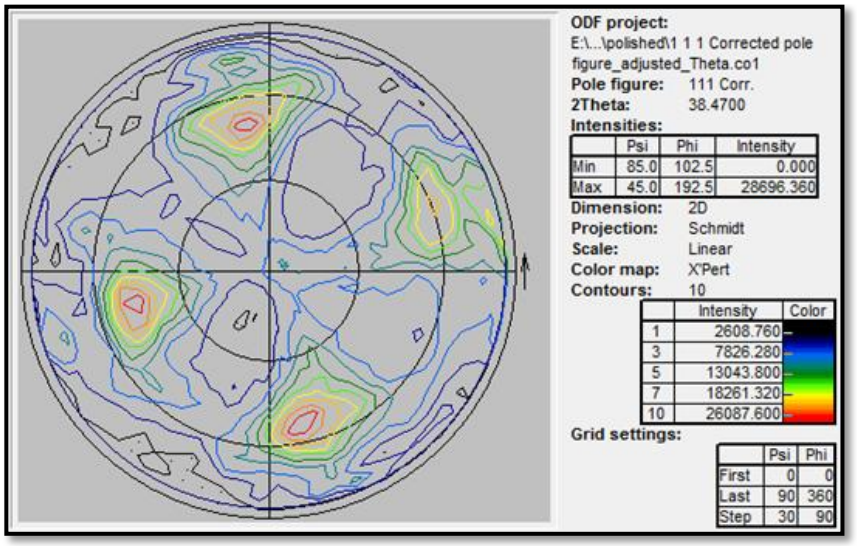

b)

(200)

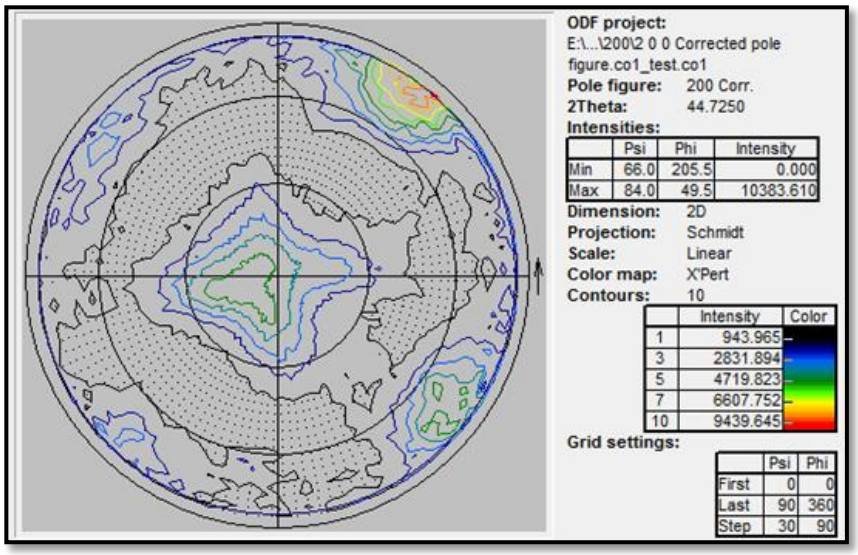

c)

(220)

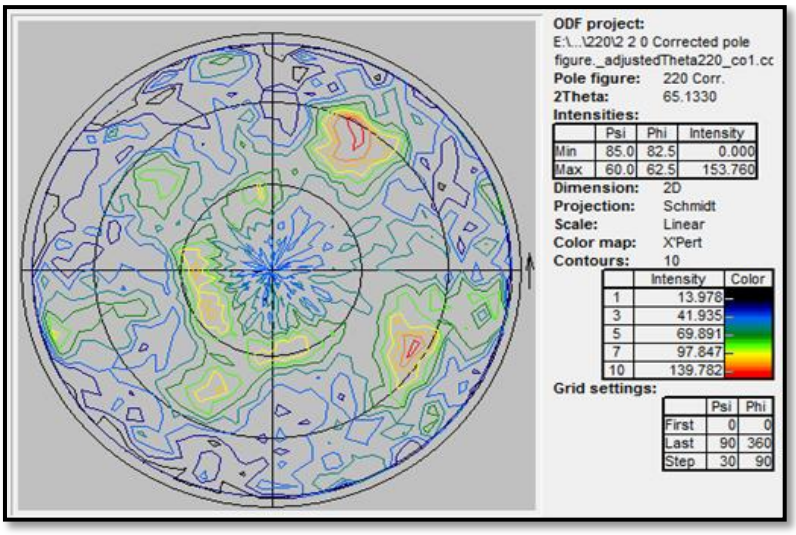

Figure 47: Pole figures for the ECAP_1 sample, a) (111) plane; b) (200) plane, and c) (220) plane.

ECAP_4:

a)

(111)

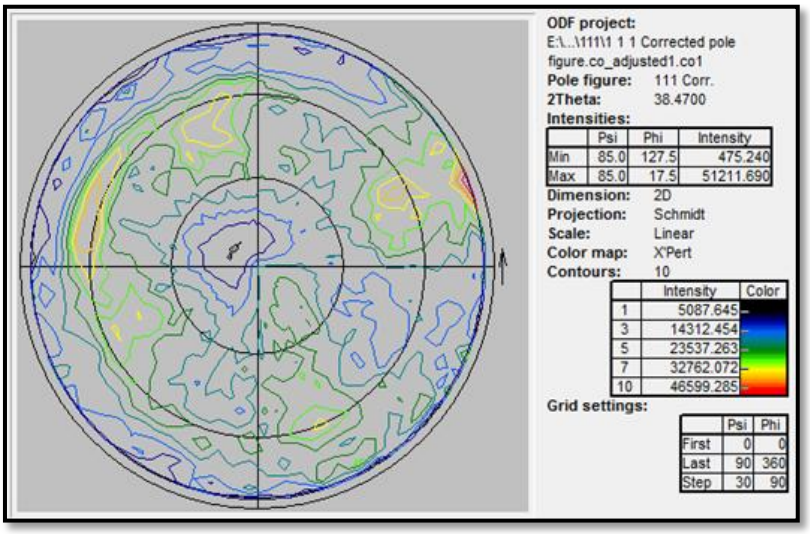

b)

(200)

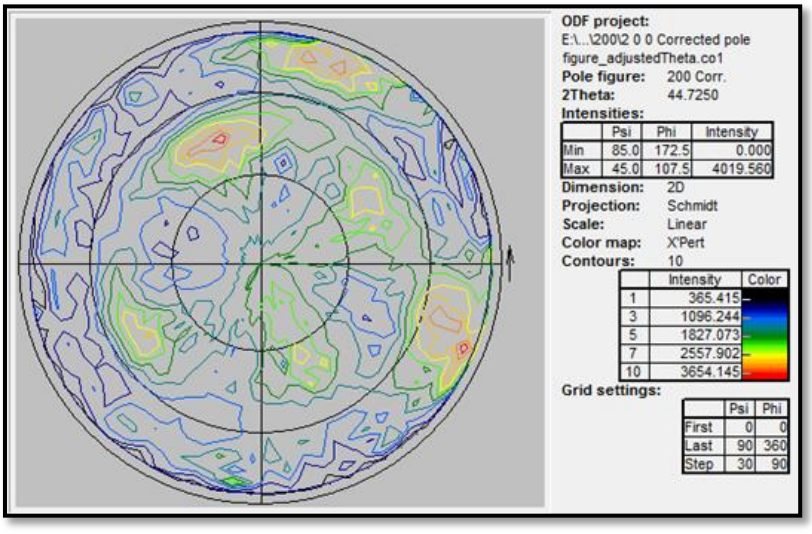

c)

(220)

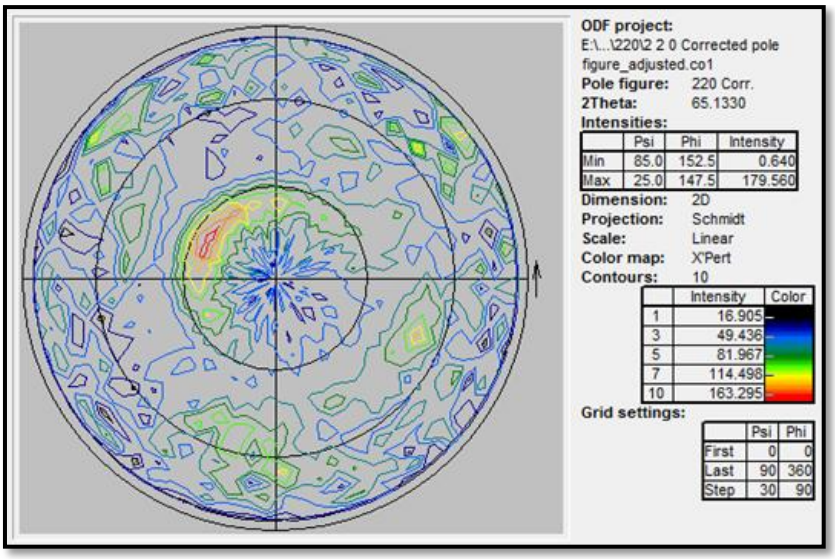

Figure 48: Pole figures for the ECAP_4 sample, a) (111) plane; b) (200) plane, and c) (220) plane.

ECAP_16:

a)

(111)

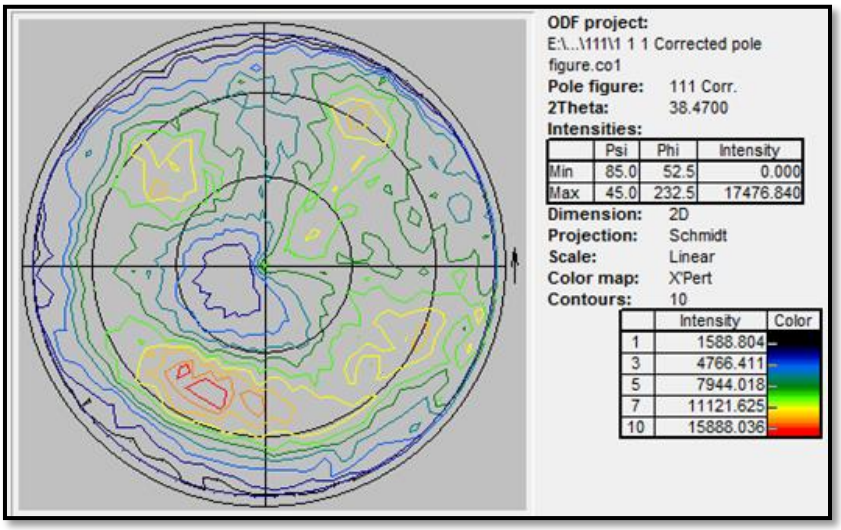

b)

(200)

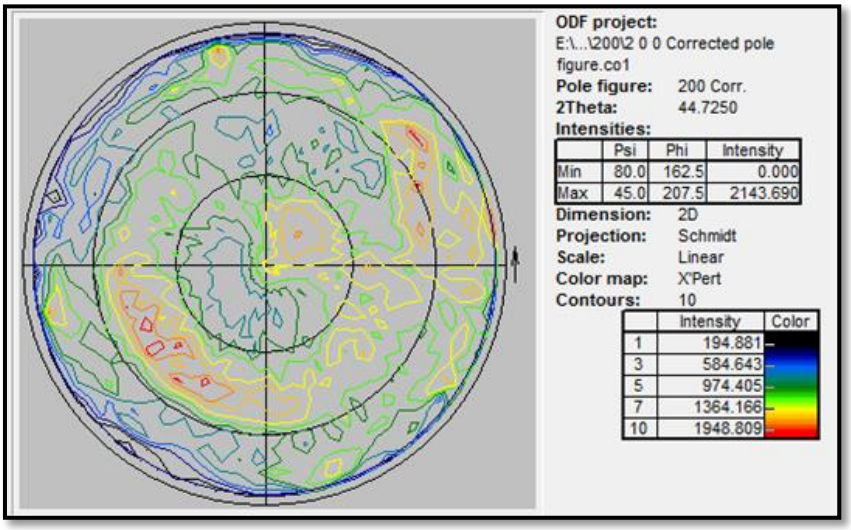

c)

(220)

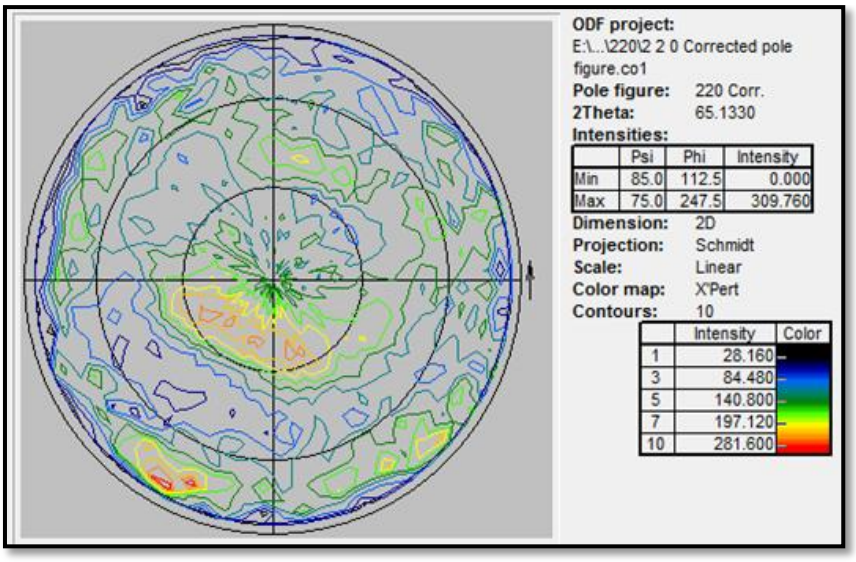

Figure 49: Pole figures of ECAP_4 sample, a) (111) plane; b) (200) plane and c) (220) plane lattice.

APPENDIX 2

Texture measurements after the compression deformation

ECAP_1:

a)

(111)

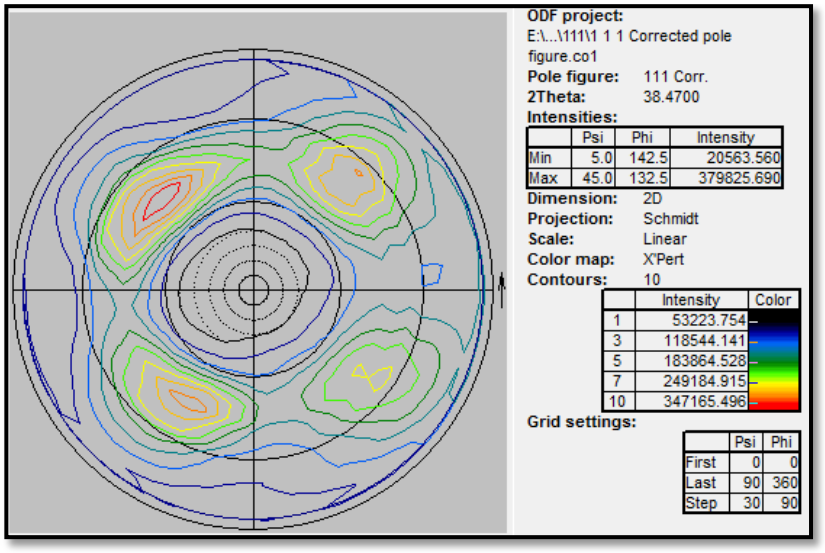

b)

(200)

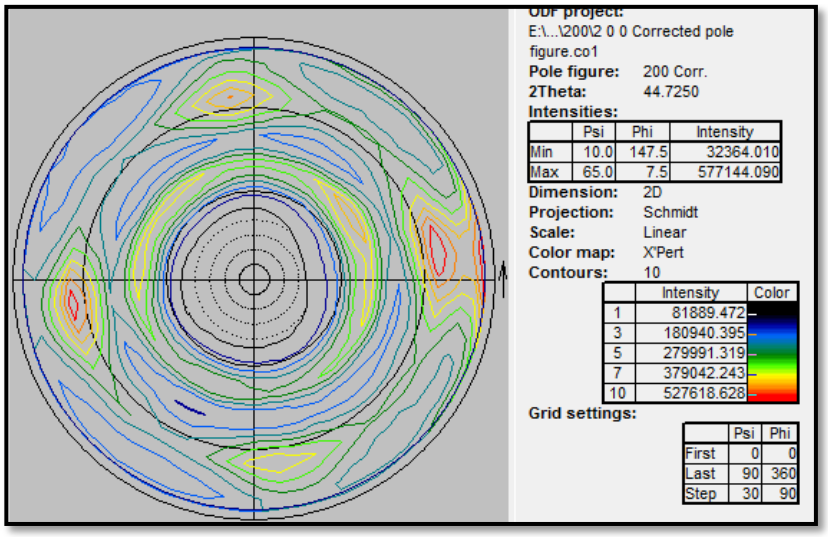

c)

(220)

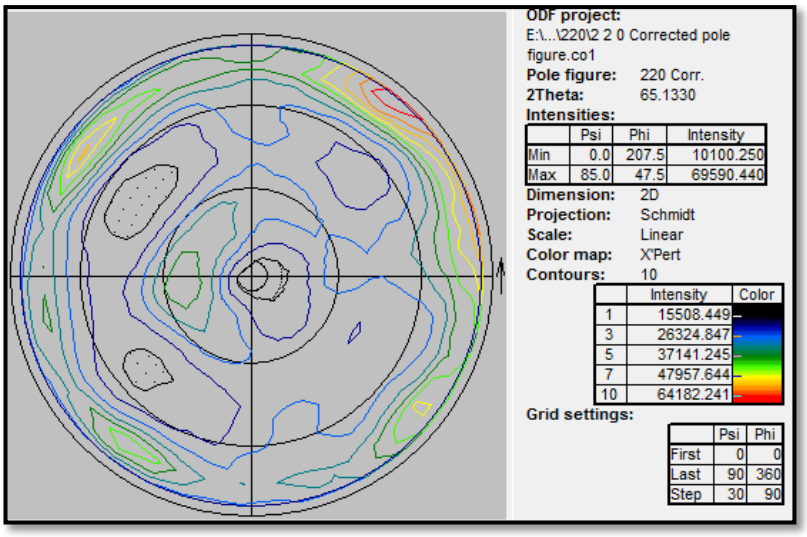

Figure 50: Pole figures of ECAP_1 sample after compression deformation, a) (111) plane; b) (200) plane and c) (220) plane.

ECAP_4:

a)

(111)

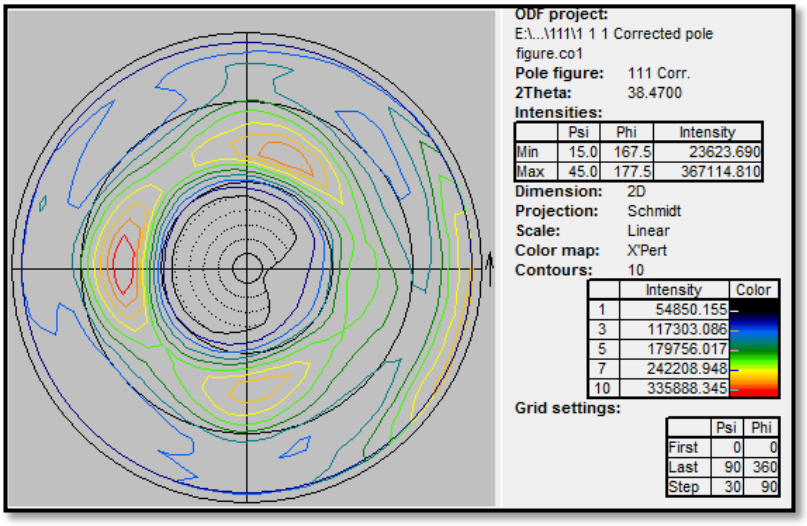

b)

(200)

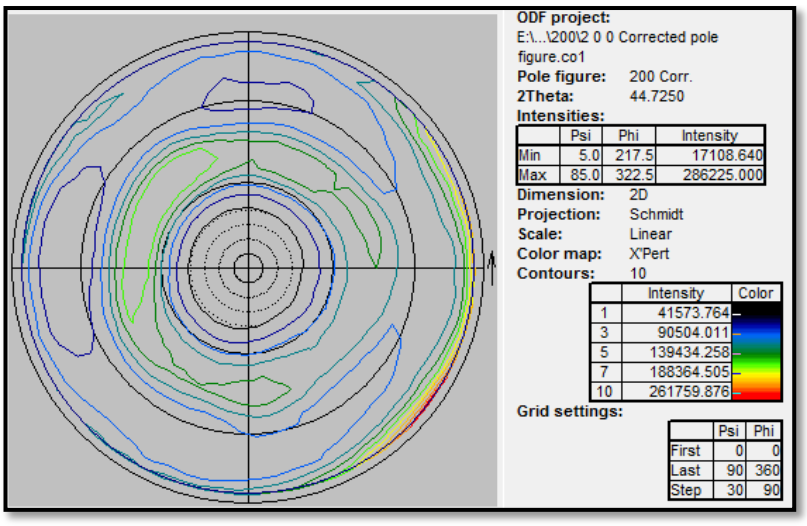

c)

(220)

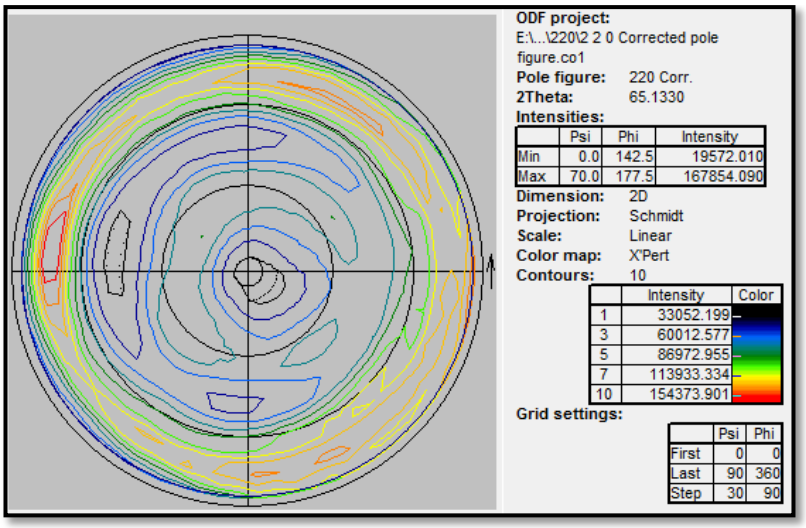

Figure 51: Pole figures of ECAP_4 sample after compression deformation, a) (111) plane; b) (200) plane and c) (220) plane lattice.

ECAP_16:

a)

(111)

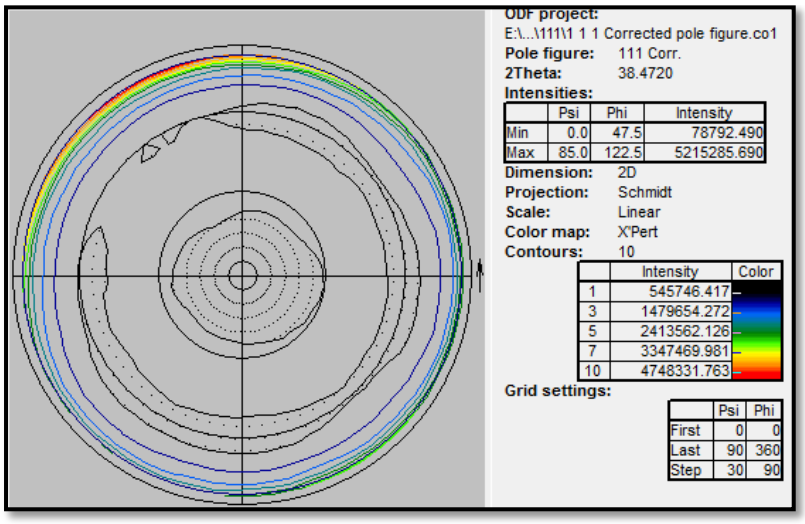

b)

(200)

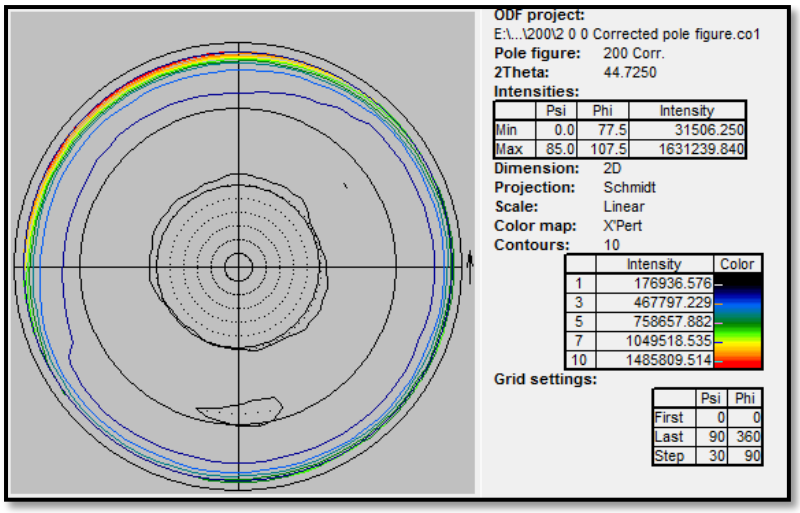

c)

(220)

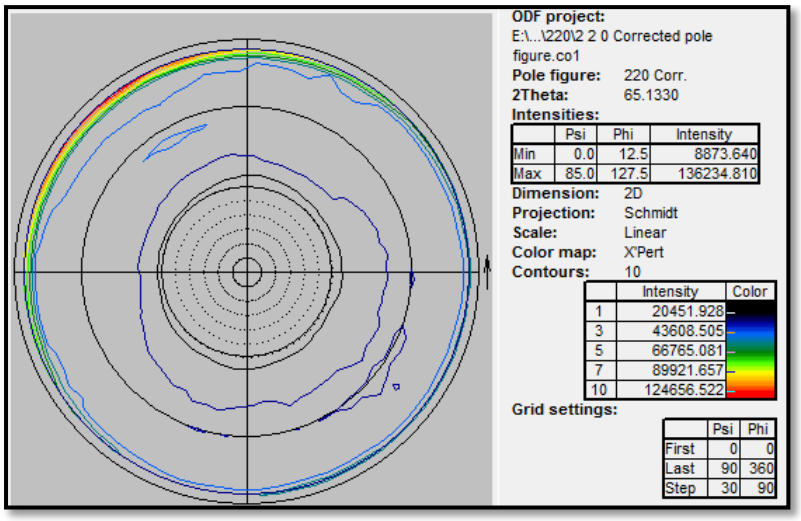

Figure 52: Pole figures of ECAP_16 sample after compression deformation, a) (111) plane; b) (200) plane and c) (220) plane lattice.

a)

(111)

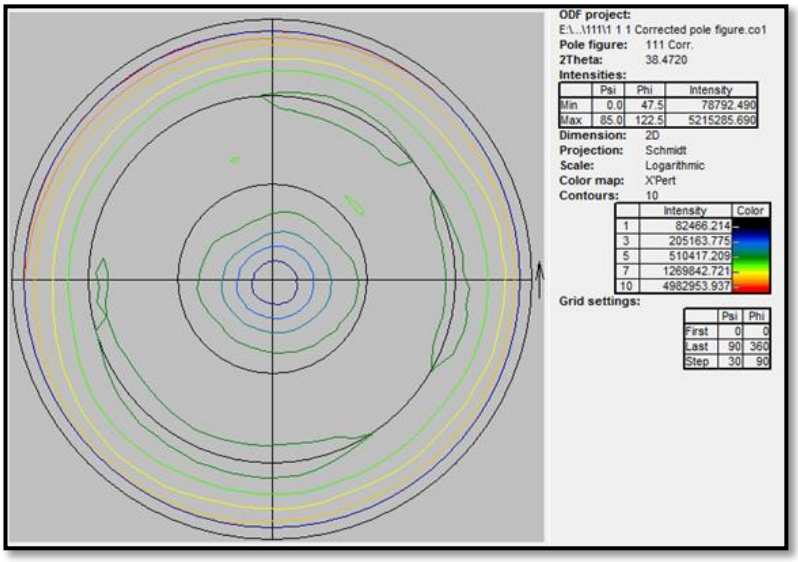

b)

(200)

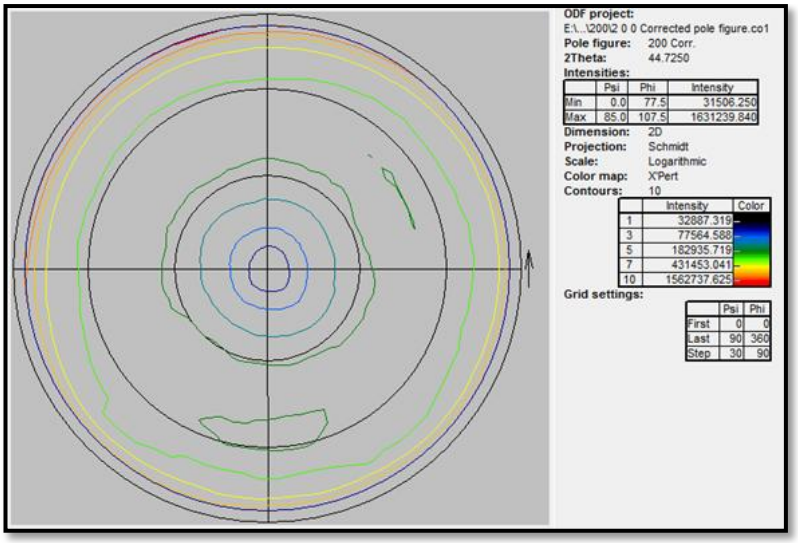

c)

(220)

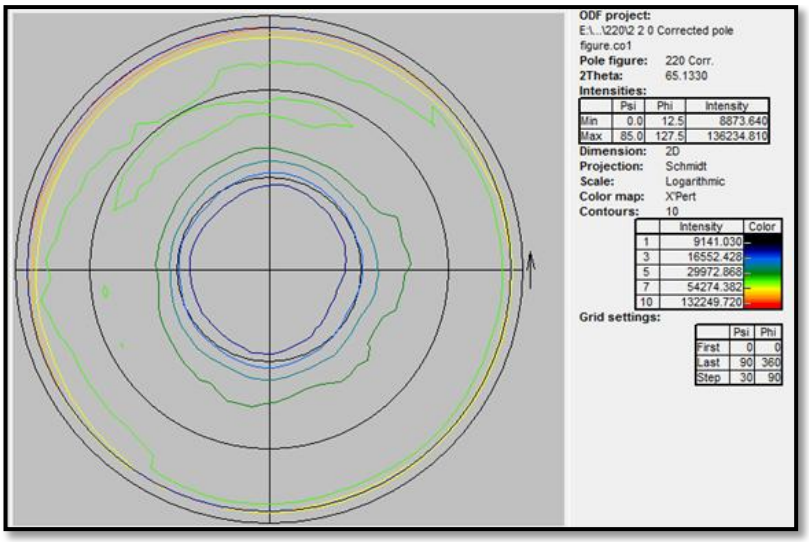

Figure 53: Pole figures of ECAP_16 sample after compression deformation in logarithmic scale a) (111) plane; b) (200) plane and c) (220) plane lattice.

APPENDIX 3

ODF results

ODF representation of the ECAP'ed samples before the compression deformation.

ECAP_1:

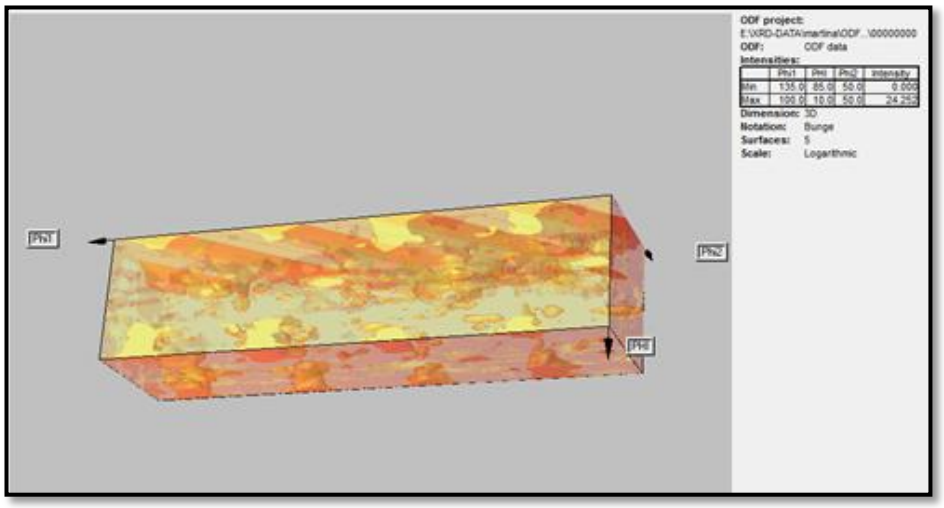

Figure 54: 3-D presentation of ODF for ECAP_1 sample.

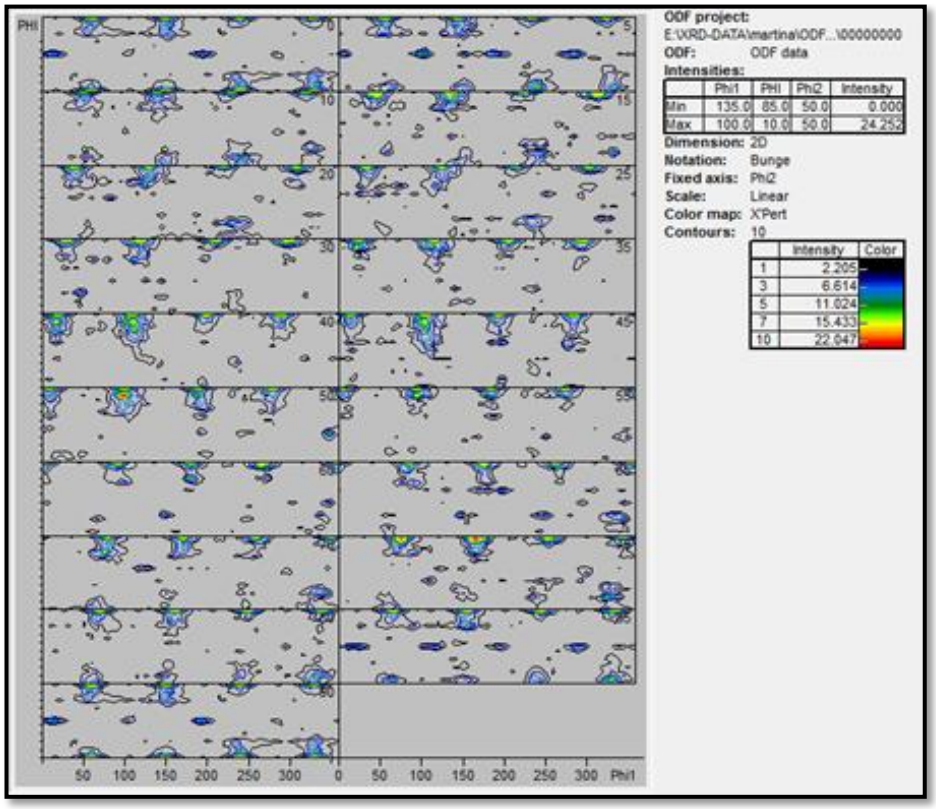

Figure 55: Complete ODF for ECAP_1 sample.

ECAP_4:

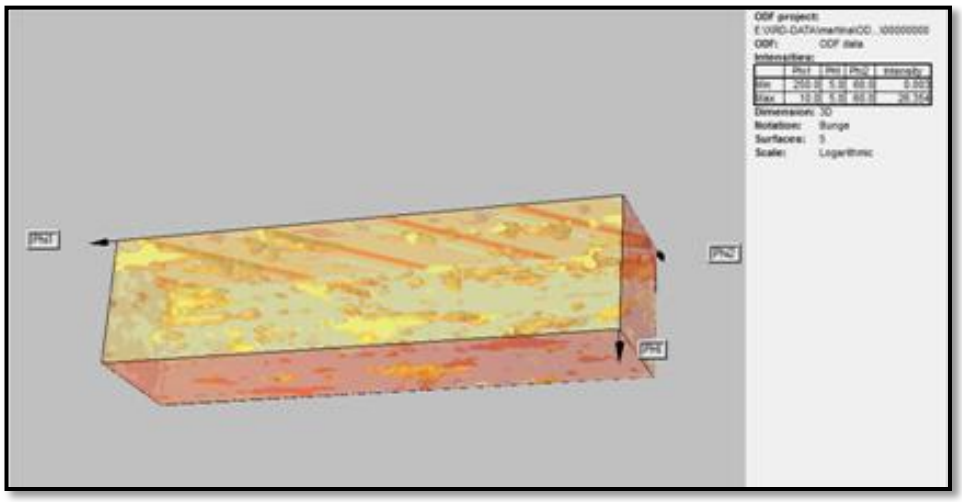

Figure 56: 3-D presentation of ODF for ECAP_4 sample.

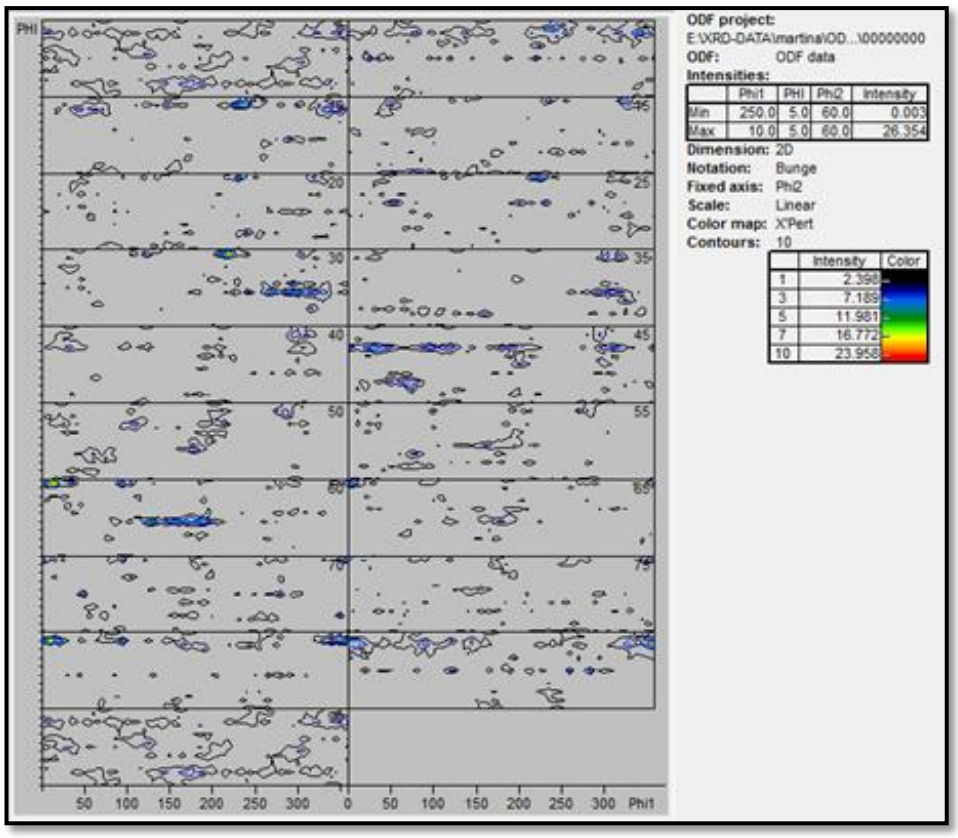

Figure 57: Complete ODF for ECAP_4 sample.

ECAP_16:

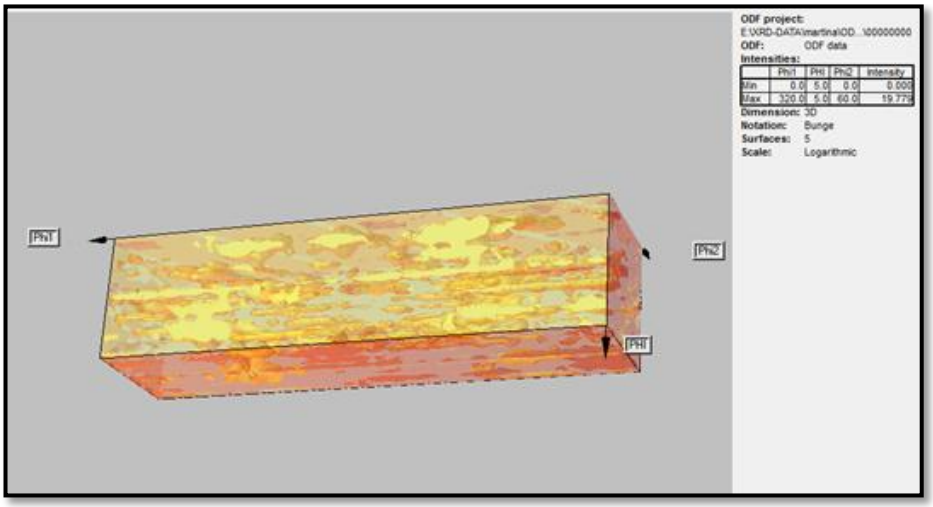

Figure 58: 3-D presentation of ODF for ECAP_16 sample.

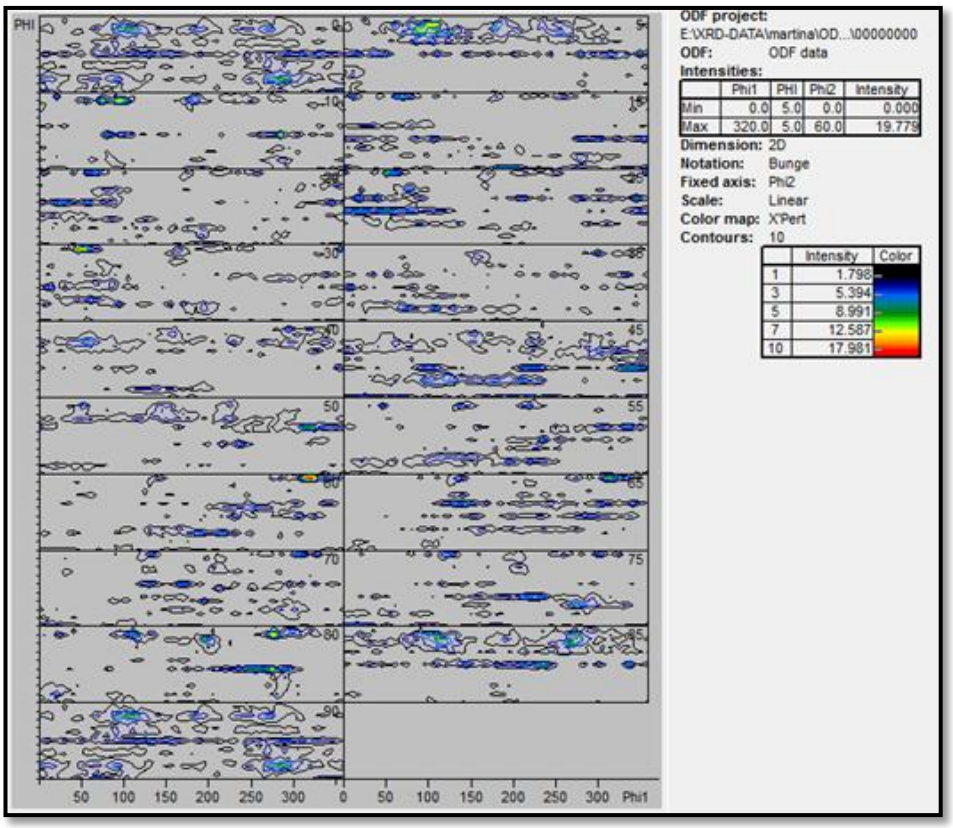

Figure 59: Complete ODF for ECAP_16 sample.

ODF representation of the ECAP'ed samples after the additional compression deformation.

ECAP_1:

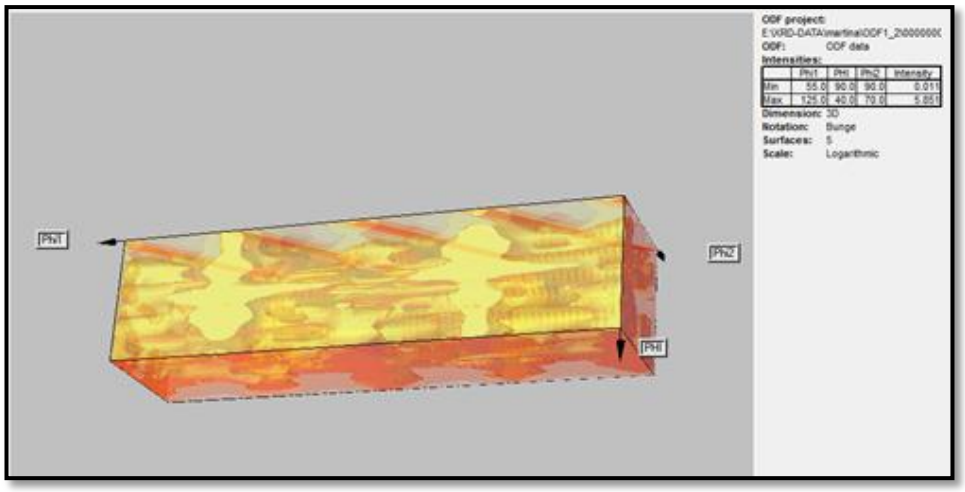

Figure 60: 3-D presentation of ODF for ECAP_1 sample.

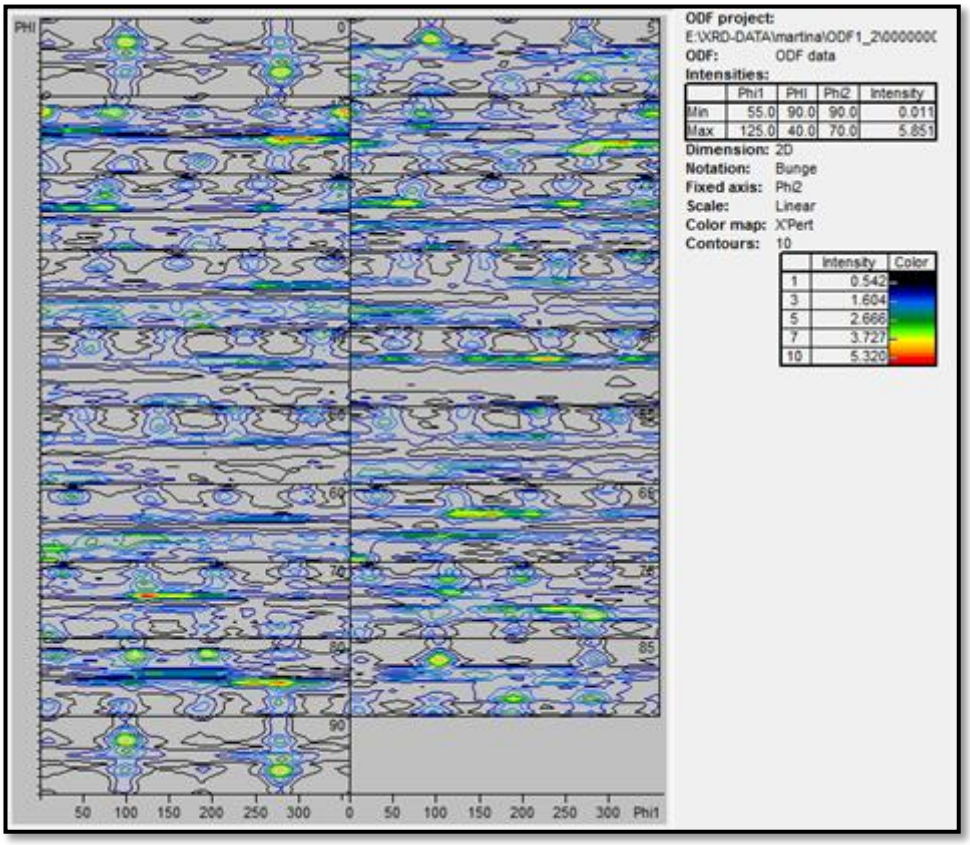

Figure 61: Complete ODF for ECAP_1sample.

ECAP_4:

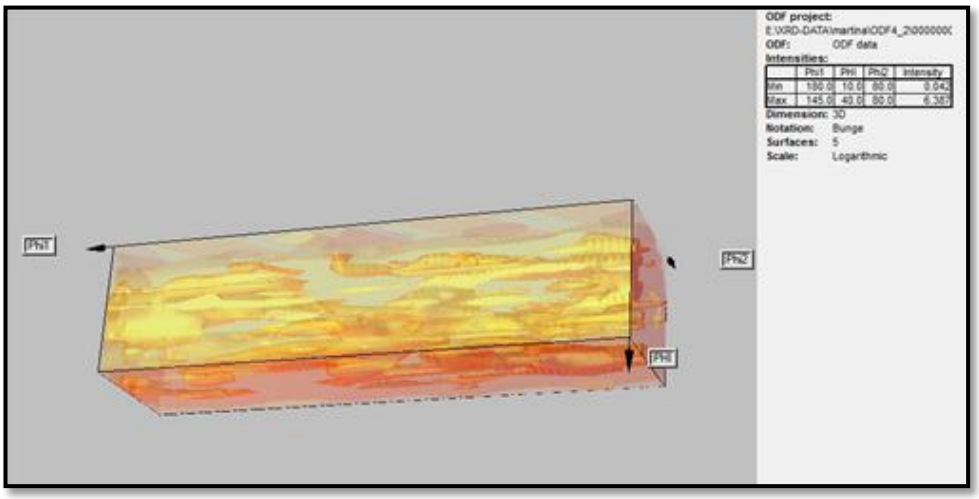

Figure 62: 3-D presentation of ODF for ECAP_4 sample.

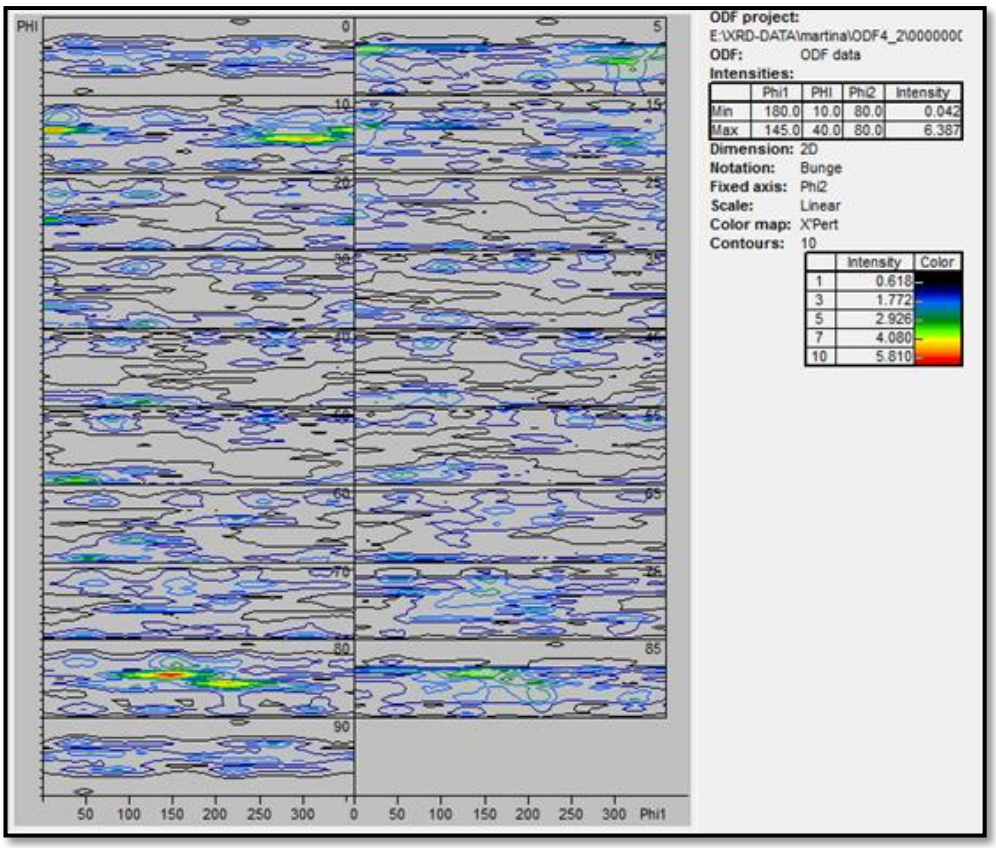

Figure 63: Complete ODF for ECAP_4 sample.

ECAP_16:

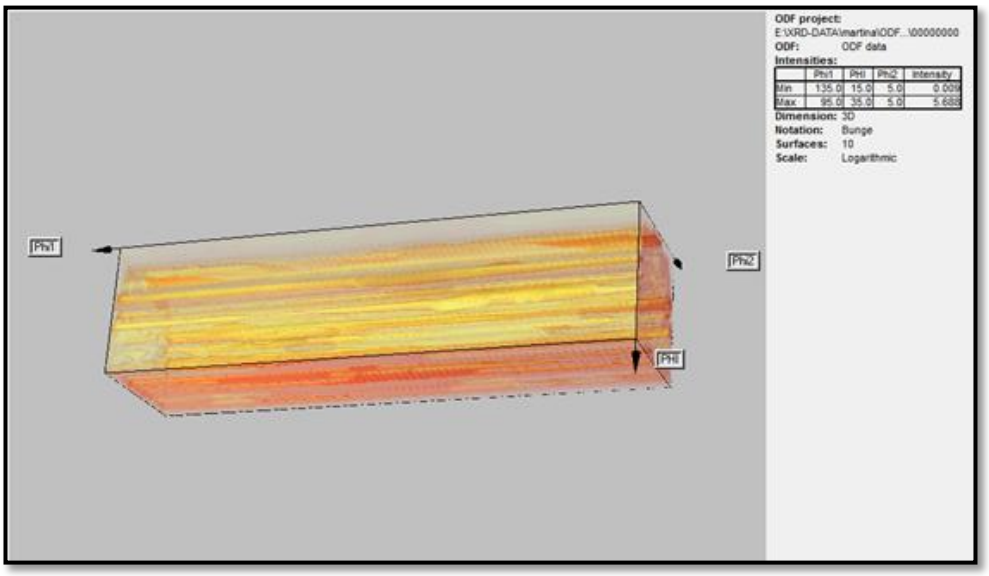

Figure 64: 3-D presentation of ODF for ECAP_16 sample.

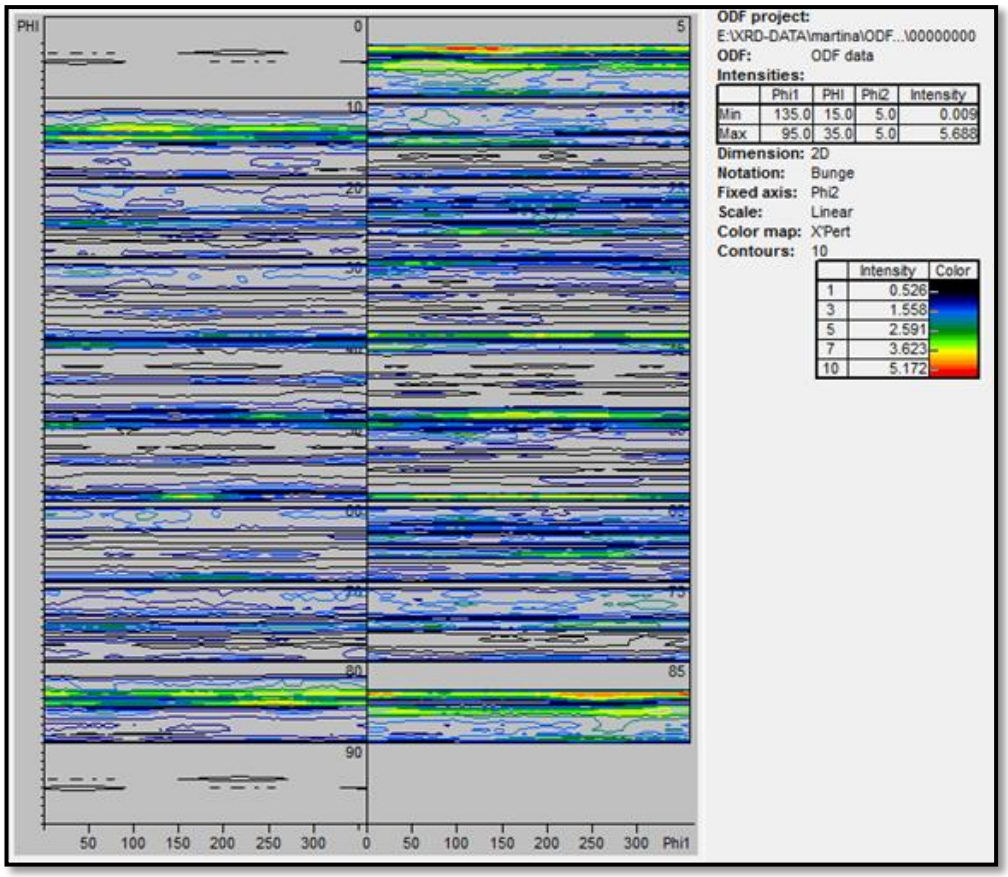

Figure 65: Complete ODF for ECAP_16 sample.

References

1. **A. Azushimaa, R. Koppb, A. Korhonenc, D.Y. Yangd, F. Micarie, G.D. Lahotif, P. Grocheg, J. Yanagimotoh, N. Tsujii, A. Rosochowskij, A. Yanagidaa.** *Severe plastic deformation (SPD) processes for metals.* 2, 2008, Vuosik. 55, ss. 716-735.

2. **R.Z. Valiev*, R.K. Islamgaliev, I.V. Alexandrov.** *Bulk nanostructured materials from severe plastic deformation.* 2002, Progress in Materials Science 45, ss. 103-189.

3. **Verlinden, Bert** *Severe Plastic Deformation of Metals*.**.** s.l. : MJOM- Metalurgija - Journal of Metallurgy, 2004, ss. 165-172.

4. **J. Zrnik, S. V. Dobatkin, I. MamuziI^.** *Procesing of Metals by Severe Plastic Deformation (SPD) – Structure and mechanical properties respond.* 3, s.l. : Meatbk, 2008, Vuosik. 47, ss. 211-216.

5. **Jurij J. Sidor*, Roumen H. Petrov, Leo A.I. Kestens.** *Microstructural and texture changes in severely deformed aluminum alloys*.**.** Belgium : Materials Characterization, 2011, Vuosik. 62, ss. 228-236.

6. **Valiev, R. Z., Krasilnikov, N. A. & Tsenev, N. K.** *Plastic Deformation of Alloys with Submicron-Grained Structure.* s.l. : Materials Science and Engineering a-Structural Materials Properties Microstructure and Processing, 1991, Vuosik. 137, ss. 35-40.

7. **Melichera, R.** *Numerical simulation of plastic deformation of aluminium workpiece induced by ECAP technology.* 2009, Applied and Computational Mechanics 3 , ss. 319-330.

8. **Segal, V. M., Reznikov, V. I., Drobyshevisky, A. E. & Kopylov, V.** *Plastic Working of Metals by Simple Shear.* s.l. : Russian Metallurgy, 1981. ss. 99-105.

9. **Berbon, P. B., Furukawa, M., Horita, Z., Nemoto, M. & Langdon,T. G**. *Influence of pressing speed on microstructural development in equal-channel angular pressing*.**.** s.l. : Metallurgical and Materials Transactions a-Physical Metallurgy and Materials Science, 1999, Vuosik. 30, ss. 1989-1997.

10. **Li S, Beyerlein IJ, Bourke MAM.** *Texture formation during equal channel angular extrusion of fcc and bcc materials:comparison with simple shear.* 94, s.l. : Materials Science Engineering A, 2005, Vuosik. 3, ss. 66-67.

11. **VM, Segal.** *Materials processing by simple shear.* s.l. : Materials Science Engineering A, 1995, Vuosik. 197, ss. 157-164.

12. **A. Gholinia b, P. Bate a, P.B. Prangnell a,∗.** *Modelling texture development during equal channel angular extrusion of aluminium.* s.l. : Acta Materialia, 2002, Vuosik. 50, ss. 2121-2136.

13. **Iwahashi, Y., Wang, J., Horita, Z., Nemoto, M. & Langdon, T. G.** *Principle of equal-channel angular pressing for the processing of ultra-fine grained materials.* 35, s.l. : Scripta Materialia, 1996, ss. 143-146.

14. **Yamashita, A., YamaguchiI, D., Horita, Z. & Langdon, T. G.** *Influence of pressing temperature on microstructural development in equal-channel angular pressing.* s.l. : Materials Science and Engineering A, 2000, Vuosik. 287, ss. 100-106.

15. **Lapovok K, R. E.** *The function of the counterpressure on equal channel angular pressing.* s.l. : Metally, 2004, ss. 44-50.

16. **S. Li a, ∗, M.A.M. Bourkea, I.J. Beyerleinb, D.J. Alexandera, B. Clausenc.** *Finite element analysis of the plastic deformation zone and working load in equal channel angular extrusion.* s.l. : Materials Science and Engineering A , 2004, Vuosik. 382, ss. 217-236.

17. **Nakashima, K., Horita, Z., Nemoto, M. & Langdon, T. G.** *Developement of a multi-pass facility for equal-channel angular pressing to high total strains.* s.l. : Materials Science and engineering A, 2000. ss. 82-87. Vuosik. 281.

18. **Lee, S. & Langdon, T. G.** *Influence of equal-channel angular pressing on the superplastic properties of commercial aluminum alloys.* s.l. : Superplasticity-Current Status and Future Potential., 2000. ss. 359-364. Vuosik. 601.

19. **Valiev, R. Z. & Langdon, T. G.** *Principles of equal-channel angular pressing as a processing tool for grain refinement.* s.l. : Progress in Materials Science, 2006, Vuosik. 51, ss. 881-981.

20. ***Robert De Angelis, Todd Snyder,Joel House and William Hosford.*** **s.l**. : Advances in X-ray Analysis, 2000, Vuosik. 42, ss. 510-520.

21. **Randle, Olaf Engler and Valerie.** *Introduction to Texture Analysis.* Florida : Taylor & Francis Group, 2010. 978-1-4200-6365-3.

22. **Wenk, H-R ja Houtte, P Van.** *Texture and anisotropy.* Belgium : Reports on Progress in Physics, 2004, Vuosik. 67, ss. 1367-1428.

23. **Rollett, A. D.** Texture, Microstructure & Anisotropy, Materials Science and Engineering . *Carnegie Mellon University*. [Online] 2014. http://neon.mems.cmu.edu/rollett/27750/27750.html.

24. **Beyerlein, I. J. & Toth, T., L. S.** s.l. : *Texture evolution in equal-channel angular xtrusion.* Progress in Materials Science, 2009, Vuosik. 54, ss. 427-510.

25. **Swisher, Douglas Lee.** *Production of ultre-fine grains and evolution of grain boundaries during severe plastic deformation of aluminum and its alloys.* s.l. : Master Thesis, Approved for public release, 2000.

26. **A.P. Zhilyaev, D.L. Swisher, K. Oh-ishi, T.G. Langdon , T.R. McNelley.** s.l. : *Microtexture and microstructure evolution during processing of pure aluminum by repetitive ECAP.* Materials Science and Engineering A, 2006, Vuosik. 429, ss. 137-148.

27. Department of Applied Physics. *The Hong Kong Polytechnics University.* [Online] 2014. http://ap.polyu.edu.hk/apakhwon/Lecture%2001%20-%20X-ray%20Diffraction.pdf.

28. **Cowley, John M.** Diffraction physics. Amsterdam : America Elsevier, 1975.

29. **Darrell Henry, Dave Mogk.** X-ray reflection in accordance with Bragg's Law. *Science Education Recearch Center.* [Online] 2012. http://serc.carleton.edu/research_education/geochemsheets/BraggsLaw.html.

30. **W.H.Bragg, W.L. and.** Cambridge Physics. *X-ray diffraction.* [Online] 2014. [Viitattu: 8. September 2014.] http://www-outreach.phy.cam.ac.uk/camphy/xraydiffraction/xraydiffraction7_1.htm.

31. **Cockcroft, Jeremy Karl.** Bragg-Brentano Parafocussing Circles. *Birckbeck College, University of London.* [Online] 2006. http://pd.chem.ucl.ac.uk/pdnn/inst1/focircle.htm.

32. **XOS.** Parallel Beam X-ray Diffraction. *XOS.* [Online] [Viitattu: 10. September 2014.] http://www.xos.com/techniques/xrd/parallel-beam-x-ray-diffraction/.

33. **Key, Prof. Thomas.** X-Ray Diffraction - Background and Fundamentals. [Online] http://www.slideshare.net/meonly21IcandependonhimallmylifeAA/xrd-lecture-1.

34. **Y.S. Liu, L. Depre, L. De Buyser, T.B. Wu, and P. Van Houtte.** *Intensity correction in texture measurements of polycrystaline thin films by x-ray diffraction.* 3/4, 2003, Textures and Microstructures, Vuosik. 35, ss. 283-290.

35. **Weaver, Prof. M.L.** The University of Alabama. *Macrotexture Macrotexture* . [Online] March 2011. http://bama.ua.edu/~mweaver/courses/MTE583/MTE%20583_Class_23.pdf.

36. **Gurao, Satyam Suwas AND Nilesh P.** *Crystallographic texture in Materials.* 2, Bangladore : Journal of the Indian Institute of Science 1, 2008, Vuosik. 88, ss. 151-177.

37. Software for quantitative X-ray texture analysis. *PANalytical.* [Online] 2014. http://www.panalytical.com/Xray-diffraction-software/Texture.htm.

38. **D. B. Knorr, H. J. Bunge.** *Proceedings from the Symposia "Textures in Non-Metallic Materials and Microstructure and Texture evolution during annealing of deformed materials.* 2+3, Indianapolis : Materials Week, 1989, Vuosik. 13. ISSN: 0730-3300.

39. **Hu, Hsun.** *Texture of metals.* Pennsylvania, USA : Texture, 1974, Vuosik. 1, ss. 233-258.

40. **Davies, RM.** 240, s.l. :*A critical study of the Hopkinson Pressure Bar.* Philos. Trans. R. Soc. (London) A, 1948, ss. 375-457.

41. **Gray, G. T.** s.l. :*Classic Split Hopkinson Pressure Bar Technique.* ASM V8 Mechanical Testing, 1999, ss. 17-20.

42. **Zhao, H., Gary, G.** *On the use of a Viscoelastic Split Hopkinson Pressure Bar.* 4, s.l. : Int J Impact Eng., Vuosik. 19, ss. 319-330.

43. **Hokka, Mikko.** *Effects of strain rate and temperature on the mechanical behavior of* . s.l. : Tampere : Tampere University of Technology , 2008.

44. **M Saravanan, R M Pillai, B C Pai, M Brahmakumar and K R Ravi** *Equal channel angular pressing of pure aluminium—an analysis.***.** 7, s.l. : Indian Academy of Sciences, 2006, Bull. Mater. Sci., Vuosik. 29.

45. **Jiri Dvorak, Vaclav Sklenicka and Zenji Horita.** *Microstructural Evolution and Mechanical Properties of High Purity Aluminium Processed by Equal-Channel Angular Pressing.* 1, s.l. : The Japan Institute of Metals, 2008, Materials Transactions, Vuosik. 49, ss. 15-19.
22888